
XRF Spectroscopy in Analytical Multi-sensor Drill Core-scanning: Evaluating the potential of Qualitative and Quantitative Analysis for Aguas Teñidas, Magdalena, Sotiel and Majada deposits, Iberian Pyrite Belt, Spain (Université de Liège)

Auteur : Zerai Semereab, Milkias

Promoteur(s) : Pirard, Eric

Faculté : Faculté des Sciences appliquées

Diplôme : Master en ingénieur civil des mines et géologue, à finalité spécialisée en "geométallurgy (EMERALD)

Année académique : 2020-2021

URI/URL : <http://hdl.handle.net/2268.2/13969>

Avertissement à l'attention des usagers :

Tous les documents placés en accès ouvert sur le site le site MatheO sont protégés par le droit d'auteur. Conformément aux principes énoncés par la "Budapest Open Access Initiative"(BOAI, 2002), l'utilisateur du site peut lire, télécharger, copier, transmettre, imprimer, chercher ou faire un lien vers le texte intégral de ces documents, les disséquer pour les indexer, s'en servir de données pour un logiciel, ou s'en servir à toute autre fin légale (ou prévue par la réglementation relative au droit d'auteur). Toute utilisation du document à des fins commerciales est strictement interdite.

Par ailleurs, l'utilisateur s'engage à respecter les droits moraux de l'auteur, principalement le droit à l'intégrité de l'oeuvre et le droit de paternité et ce dans toute utilisation que l'utilisateur entreprend. Ainsi, à titre d'exemple, lorsqu'il reproduira un document par extrait ou dans son intégralité, l'utilisateur citera de manière complète les sources telles que mentionnées ci-dessus. Toute utilisation non explicitement autorisée ci-avant (telle que par exemple, la modification du document ou son résumé) nécessite l'autorisation préalable et expresse des auteurs ou de leurs ayants droit.



Université de Liège - Faculté des Sciences Appliquées

XRF Spectroscopy in Analytical Multi-Sensor Drill Core-Scanning:
Evaluating the Potential of Qualitative and Quantitative Analysis for Aguas
Teñidas Deposit, Iberian Pyrite Belt, Spain

This thesis is submitted in partial fulfillment of the requirements for the EMerald triple degree

« Master in Mining and Geological Engineering » from University of Liège

« Master in Sciences de la Terre et des Planètes Environnement » from L'École Nationale
Supérieure de Géologie, University of Lorraine, Nancy

« Master in Mechanical and Process Engineering » from Technische Universität
Bergakademie Freiberg

Presented by

Milkias Zerai Semereab

The thesis is confidential - data may only be used with the written consent of the thesis
supervisor:

Eric Pirard (ULg)

Academic Year 2020-2021



[This page was intentionally left blank]

ACKNOWLEDGEMENTS

First of all, my appreciation to the EMerald consortium for creating, organizing and maintaining such prestigious program and for making everything possible during those 2 years despite the pandemic. It was great opportunity to attend such broad-based courses at the University of Liège, University of Lorraine, and TU Bergakademie Freiberg, I thank you all for everything.. Thanks also to all the classmates and friends who made this two-year journey worthwhile.

I would like to thank my principal thesis supervisor prof. Eric Pirard for the eye-opening lectures in the area of process mineralogy and application of sensors in the raw material sciences. The courses have already changed the path of my professional career. Moreover, thank you for guiding and supervising my thesis works during these last months. I would also like to thank the GeMMe research team; Pierre Barnabé and Pierre-Henri Koch for their useful input to my thesis. And Special thanks to Hassan Bouzahzah (PhD) for providing me practical guidance and spending long hours at the SEM Lab analyzing samples.

I would like to sincerely acknowledge the hospitality rendered to me by DMT GmbH. My special thanks to Carlos García Piña, Analytical Core Logging (ANCORELOG) project coordinator at DMT GmbH who provided me guidance and support in every step of this work. I appreciate his patience, kindness and constant availability for support.

I wish to extend my special thanks to Fanuel Mehari who has provided me essential information regarding thesis writing and applications of spectroscopy in raw materials.

I offer my regards to my family, friends, and colleagues who supported me in many ways during the completion of the program. Finally my sincere acknowledgement to all my teachers who taught me from elementary school till my post-grad, thank you all for shaping me all the way into who I am now.

“Meron, my late brother, my hero, my maestro. Although your dream was cut short, I hope I did little to compensate the loss by bringing another degree to the family. R.I.P.”

[This page was intentionally left blank]

ABSTRACT

During exploration of mineral resources, extensive drilling campaigns are conducted involving a considerable amount of expenses and time. Drill core logging is then carried out by geologists to evaluate the resource. However, this methodology is often subjective, non-standardized and time-consuming. As novel sensors are released into the market, automated logging technologies are set to solve this constraint by developing drill core scanning prototypes.

This master thesis is part of ANCORELOG project (Analytical Core Logger); EIT Raw Materials supported project that aims to develop and commercialize a multi-sensor automated drill core logging system with state-of-art technology. ANCORELOG have, so far, successfully implemented Short-Wave Infrared (SWIR) camera for supervised classification of drillcore segments into geological domains using machine learning algorithms. However, the integration of new sensors to the system such as XRF, RAMAN or LIBS will enhance the capability of ANCORELOG by providing real-time qualitative and quantitative elemental analysis.

This study focuses mainly on the spectral analysis and calibration of the X-Ray Fluorescence (XRF) sensor for evaluating the potential of qualitative and quantitative elemental analysis of drillcore samples from Iberian Pyrite Belt (IPB), Spain, where the Aguas Teñidas, Magdalena and Sotiel mines of Cu-Pb-Zn are explored by Minas de Aguas Teñidas S.A. (MATSA).

The raw XRF spectra generated were analyzed and processed with the combined use of classical visual interpretation and algorithms to estimate and remove background noise as well as Gaussian method for peak-fitting. The resulting spectra showed well defined peaks that were assigned to their respective elements. Therefore, the study showed that the ANCORELOG mounted XRF sensor was successful in identifying all elements within the sensor detection limit range.

Furthermore, attempt was made to provide a means of calibrating the sensor in order to convert the measured fluorescent x-ray intensity to the actual chemical composition of the sample. Linear-regression models have shown sufficient predictive power.

The generated XRF spectra were only effective in identifying and semi-quantitatively determining sample compositions but was also able to discriminate between rock types (both mineralized and barren) with good level of accuracy with the aid of machine learning (supervised) algorithms.

Keywords: Automated Core-Scanning, Iberian Pyrite Belt, X-Ray Fluorescence, XRF Spectra Processing, XRF Calibration, Machine Learning.

TABLE OF CONTENTS

ACKNOWLEDGEMENTS	iv
ABSTRACT	vi
TABLE OF CONTENTS	vii
LIST OF SYMBOLS AND ABBREVIATIONS.....	ix
LIST OF FIGURES.....	x
LIST OF TABLES	xii
1. INTRODUCTION	1
1.1. Statement of the problem	2
1.2. Objectives and Scope of the study	3
2. LITERATURE REVIEW	5
2.1. MATSA Deposit in the Iberian Pyrite Belt.....	5
2.1.1. Geological Setting	6
2.1.2. Regional Stratigraphy	7
2.1.3. Iberian Pyrite Belt Genesis Model.....	9
2.1.4. Metallogeny	10
2.1.5. MATSA Mining and Mineral Processing Operations	11
2.2. X-Ray Fluorescence (XRF).....	13
2.2.1. Historical and Scientific Background.....	13
2.2.2. Fundamentals of X-Ray Fluorescence.....	14
2.2.3. X-Ray Fluorescence in Atoms.....	15
2.2.4. X-Ray Tube (Generation of X-Rays)	16
2.2.5. Bremsspektrum (Continuum) and Characteristic Radiation of Anode Material	18
2.2.6. Interactions of Incident X-Rays with Sample Material	20
2.2.7. Detection of X-Rays	21
2.2.8. Interpretation of XRF Spectra and Classical Analysis	23
2.2.9. Extracting XRF Analytical Results and Matrix Effect.....	25
2.2.10. Sample Preparation for XRF Analysis.....	26

2.2.11. XRF Calibration and Matrix Effect Correction	28
2.3. Drill-Core Scanning.....	30
2.3.1. Why Develop Drill-Core Scanning?	30
2.3.2. Commercial Drill Core Scanners	31
3. MATERIALS AND METHODS	35
3.1. Samples Analyzed.....	35
3.1.1. Drillcore Sampling	35
3.1.2. Samples description.....	36
3.2. XRF Instrumentation.....	37
3.2.1. XRF Hardware Equipment (J&C Bachmann TEXAS)	37
3.2.2. Software Suite	38
3.3. ANCORELOG Core-Scanning Prototype.....	40
3.4. SEM Image Acquisition (ZEISS Mineralogic)	43
4. DATA ANALYSIS AND XRF SPECTRA PROCESSING	45
4.1. XRF Spectra Qualitative/Energy Calibration.....	45
4.2. XRF Spectra Processing.....	46
5. RESULTS AND DISCUSSION	49
5.1. Supervised Classification of Lithologies Based on XRF Spectra	49
5.1.1. Defining Datasets, Classes and Features	49
5.1.2. Training and Testing (Validation)	51
5.2. Calibration of TEXAS XRF Sensor for Quantitative Analysis.....	52
6. CONCLUSION AND RECOMMENDATIONS	55
7. EIT RAW MATERIALS CHAPTER.....	57
7.1. Impact, Economic Benefits and Sustainability	57
7.2. Business Opportunities.....	58
7.3. Timegated Raman for Exploration (T-REX) and Other Future Works.....	59
APPENDICES	61
BIBLIOGRAPHY	73

LIST OF SYMBOLS AND ABBREVIATIONS

ANCORELOG	Analytical Core Logger
CPS	Counts Per Second
CRM	Certified reference material
ICP-MS	Inductively coupled plasma mass spectrometry
e-	electron
EIT	European Institute of Innovation & Technology
EDS	Energy Dispersive Spectroscopy
HIS	Hyperspectral Imaging
IBP	Iberian Pyrite Belt
MATSA	Minas de Aguas Teñidas SAU
P-XRF	Portable X-Ray Fluorescence
R&D	Research and development
SEM	Scanning Electron Microscope
T-REX	Timegated Raman for Exploration
UV	Ultraviolet Rays
VSC	Volcano-Sedimentary Complex
XRF	X-Ray Fluorescence

LIST OF FIGURES

Figure 1. Scope of the thesis	3
Figure 2. Iberian Pyrite Belt with its major high grade deposits and operations	5
Figure 3. Geological setting of the IPB along with the different zones and major deposits (Martin-Izard et al., 2015).	6
Figure 4. Simplified stratigraphic column of the IPB (Martin-Izard et al. 2016).....	8
Figure 5. Two mineralization systems in the IPB (Tornos, 2006).	9
Figure 6. Optical microscope images of polymetallic mineralizations from several massive sulfide deposits of the Iberian Pyrite Belt (Almodóvar et. al. 2019).....	11
Figure 7. Simplified mineral processing flowsheet (MATSA, 2016).	12
Figure 8. The electromagnetic spectrum (Wikipedia, 2021)	14
Figure 9. Generating X-Ray Fluorescence in an atom (Niton, 2021).....	15
Figure 10. X-Ray radiations labeling	16
Figure 11. X-Ray Tube components	18
Figure 12. Spectrum emitted by a Mo x-ray tube with 30 kV accelerating voltage and 0.5 mA electron current (Bruker, 2016)	19
Figure 13. Different types of secondary X-rays emissions; fluorescence, transmission and scatterings (R Scholtz et. al. 2006).....	20
Figure 14. Types of Interactions between an X-ray photon and the atom of irradiated matter for x-ray beam energy (Seibert J.A and Boone J.M., 2005).....	21
Figure 15. Basic components of Energy-Dispersive XRF	22
Figure 16. Typical spectrum of certified reference material (Mahuteau, 2008).....	23
Figure 17. Sum and escape peaks in XRF spectrum	24
Figure 18. Secondary enhancement of aluminum by silicon atoms (Bruker, 2006)	26
Figure 19. Most common ways to prepare samples for XRF analysis	26
Figure 20. Inter-element matrix effects (absorption and enhancement) (Bruker, 2017).	28
Figure 21. DMT manufactured CoreScan ³ (DMT Group, 2021)	32
Figure 22. MINALYZER CS (Sjöqvist et. al. 2015).....	32

Figure 23. OreXplore Geocore X10 (Orexplore, 2021)	33
Figure 24. TERRACORE SisuMobi (TerraCore Geospectral Imaging, 2021).....	33
Figure 25. Corescan HCL (Corescan, 2021)	34
Figure 26. LIBS-XRF core scanner prototype developed by SPECTRAL Industries and Avaatech’s XRF core scanner (Dalm et. al. 2019).....	34
Figure 27. Rock pieces sliced from the main drill-core samples.....	36
Figure 28. Interior of TEXAS sensor box. This box contains an x-ray tube (rear of box, with yellow warning label), an energy-discriminating detector (front of box) and a cooling system.....	38
Figure 29. TEXAS module for signal processing functions.....	39
Figure 30. TEXAS module for calibration functions	39
Figure 31. ANCORELOG Prototype (DMT, 2021).....	40
Figure 32. ANCORELOG multi-sensor unit (DMT, 2021)	41
Figure 33. Rock pieces sliced from the main drill-core samples (prepared for XRF scanning)	42
Figure 34. Laser height profile map	42
Figure 35. ZEISS Mineralogic Scanning Electron Microscope	43
Figure 36. XRF spectra that requires Energy calibration.....	45
Figure 37. Energy calibration curve	46
Figure 38. Raw and processed spectrum	47
Figure 39. XRF spectra processing and analysis.....	47
Figure 40. Scatter plot of Fe ($K\alpha$) versus Cu ($K\alpha$) + Zn ($K\alpha$) + Pb ($L\alpha$).....	51
Figure 41. Calibration procedure diagram.....	53
Figure 42. Copper, zinc, lead and iron calibration curves (measured peak intensity values versus portable XRF weight %). Note: the curves for Cu, Zn and Pb are not straight because the linear-regression are plotted on log-scale.....	54
Figure 43. Timegated Raman for Exploration (T-REX) (VTT, 2020).....	59

LIST OF TABLES

Table 1. MATSA deposit lithological classification	35
Table 2. Device specifications of the TEXAS XRF	37
Table 3. Operation Settings selected for XRF sensor scanning.	41
Table 4. ZEISS Operating parameters.....	44
Table 5. Selected peaks and their corresponding channel No. and KeV.....	46
Table 6. Dataset for supervised classification	50
Table 7. Features' ranking based on Gain Ratio.	51
Table 8. Classifiers accuracy.....	51

1. INTRODUCTION

Minerals and metals have been essential components for the growth of human society since ancient civilizations. To fulfill such needs, prospecting and exploration of mineral resources are crucial phases of raw material value chain. The main objective of mineral exploration is to discover and acquire a maximum number of economic mineral deposits at a minimum financial costs and within minimum time. Increasing global demand for raw materials and growth of industrial output are contributing to the acceleration of mineral exploration. This growth will inevitably continue in the future.

Since near-surface and easily-exploited deposits have been discovered, mined and extracted over the centuries, the search for new mineral resources has to rely on more sophisticated, cost-friendly, time-saving and technology-based prospecting and exploration techniques. This creates both opportunities and challenges to the industry which directly paves the way for researches and innovations in the field of raw materials. Thus, the mineral industry and the academic community have consolidated efforts together to develop promising innovations into applications that shape the mineral exploration of today and future. Such R&D efforts are being driven by state-of-the-art exploration techniques, sensor-based characterization of mineral resources, computer and data sciences as well as speedier and more accurate analytical methods.

This work is part of a project funded by the European Institute of Innovation & Technology (EIT) Raw Materials known as ANCORELOG - Analytical Core Logging System. Having DMT GmbH & Co. KG as leading partner, the project is a partnership between several universities, research institutes as well as exploration and mining companies (see Appendix I. for list of the consortium). ANCORELOG, a mobile drill core logging system, aims at optimizing the procedure for measuring chemical, physical and structural rock properties with high accuracy that significantly reduces time and costs while improving the prospecting and exploration performance with an automated logging methodology. ANCORELOG is based on applications of a multi-sensor instruments (SWIR camera, RGB camera, XRF sensor, LIBS sensor and Raman sensor) as well as smart machine learning classification algorithms that convert measured properties into geological, geotechnical and geometallurgical domains (classes) on-site in real-time supporting and speeding-up decision making. ANCORELOG have successfully implemented a Short-Wave Infrared (SWIR) camera into the drillcore scanning prototype for supervised classification of core segments into geological domains using machine learning algorithms. However, the integration of a new sensor (i.e. XRF) to the drillcore scanning prototype is expected to add a quantitative elemental analysis and an innovative digitalization concept to the automation of logging. This master thesis, part of ANCORELOG

project, focuses mainly on the X-ray fluorescence (XRF) sensor for evaluating the potential of qualitative and quantitative elemental analysis. The research was undertaken at the DMT GmbH & Co. KG (Essen, Germany) where the ANCORELOG prototype is being assembled and at Génie Minéral, Matériaux et Environnement (GeMME) research group at the University of Liège (ULg) using ZEISS Mineralogic (SEM) to assist the calibration of the XRF sensor. The drillcore samples used for this research are from Iberian Pyrite Belt (IPB), Spain, where the Aguas Teñidas, Magdalena and Sotiel mines of Cu-Pb-Zn are explored by Minas de Aguas Teñidas S.A. (MATSA).

1.1. Statement of the problem

Traditionally, drill core logging has been carried out by geologists using visual inspection to support exploration for mineral resources. Despite providing important basic information, this methodology can be subjective, non-standardized and time-consuming. In the recent years, new technologies have arisen to solve such exploration constraints. As sensors are released onto the market, research studies set innovative solutions to develop sensor-based drill core scanning prototypes for mineral resource exploration. The development of new core-scanning equipments along with image analysis methodologies have digitalized databases in order to enhance the acquisition, storage and interpretation of drill core data. ANCORELOG aims to offer such multi-sensor automated drill core logging system with state-of-the-art technology as a promising tool for the optimization of exploration procedures.

An important procedure of core-logging is the labelling of pieces of drillcore into geological domains. Previous ANCORELOG researches by the academic and industrial partners contributed to develop an automated system that can perform this geological logging using hyperspectral imaging (HSI). For improving the capability of ANCORELOG, previous researches concluded that additional sensors would be required to achieve the objectives. In this case, X-Ray Fluorescence (XRF) can be a complementary technology to improve decision making to HSI classification results. Moreover, the addition of important chemical information provided by the XRF sensor can enable the end-user characterize the samples better. Therefore, this thesis can be seen as a follow-up to the research works previously performed under the ANCORELOG projects.

1.2. Objectives and Scope of the study

An automated core-logging system fits perfectly into the increasingly developing concept of geometallurgy. The major goal of geometallurgy is predicting processing behavior of a mineral resources based on mineralogical (both physical and chemical) properties. An automated core-logging system could be an extremely useful tool to perform such evaluations early on in the value chain. Using a combination of sensors, mineralogical and chemical compositions can be measured and used to classify rocks into geological and geometallurgical domains. These domains provide early data that can be very relevant to reserve estimation, mine planning and processing plant design. This work will evaluate the integration of XRF sensor into the ANCORELOG prototype and its quantitative and qualitative calibration. The general scope of the thesis is shown in Figure 1.

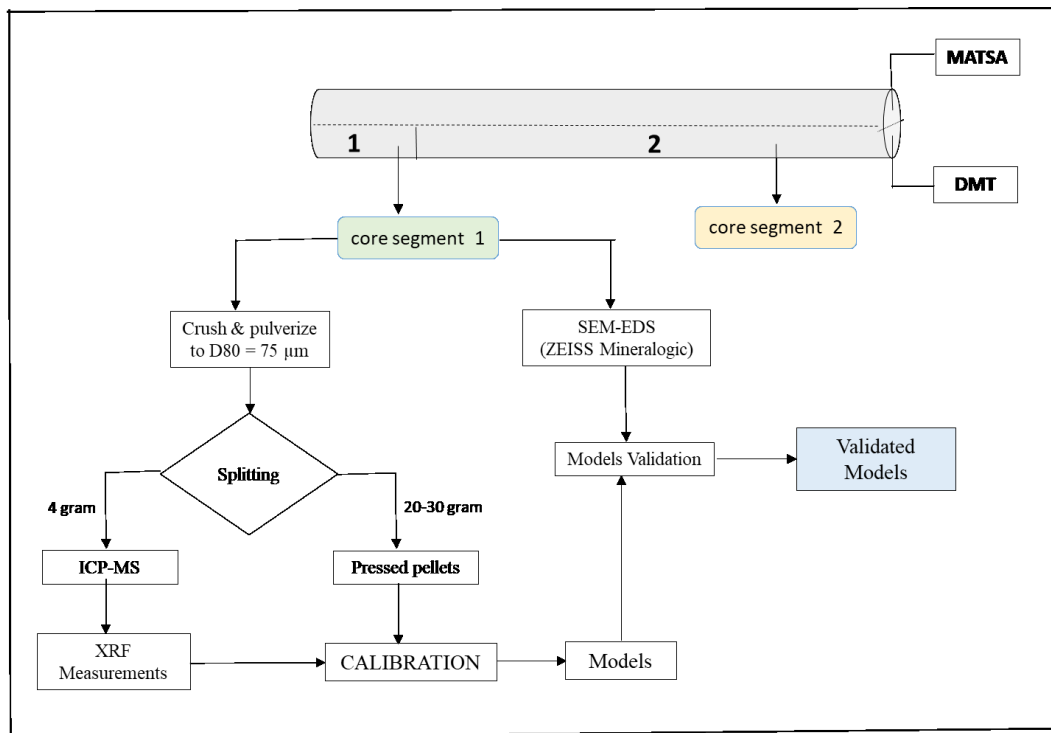


Figure 1. Scope of the thesis

The main objectives of the work can be summarized as following:

- First, all the 200 drill core samples from MATSA Iberian Pyrite Belt deposit will be inspected at DMT GmbH with visual logging. The classification of the samples into 14 lithologies, which was already done in the early stage of the project, will be carefully reviewed.
- The XRF sensor manufactured by J&C Bachmann will be set up into the Analytical Core Logger (ANCORELOG prototype).
- Subsequently, all small core segments (indicated as core segment-1 in Figure 1) will be scanned with the XRF sensor with variable operating and sensor settings.

- The raw and noisy XRF spectra will be processed into well-defined Gaussian-fitted elemental peaks and thus identification and quantification of elemental composition will be performed.
- Based on the XRF spectra (peak energy and peak intensity), qualitative models will be developed for elemental identification. Moreover, samples to be sent to laboratory for chemical analysis will be selected following a systematic protocol to ensure that all types of lithologies and the whole range of chemical composition for all elements of interest is represented.
- Calibration of the sensor will be attempted by developing Linear-regression calibration models to convert the XRF output (count rate) to element concentrations based on known composition samples (laboratory chemical analysis results) and pressed pellets XRF measurements.
- Moreover, Supervised classification of drill core samples into basic lithological classes will be carried out using XRF spectral features
- Finally, one core samples per each lithology (and three for the massive sulfide) will be analyzed by scanning electron microspore (ZEISS Mineralogic). The same samples will be also analyzed with the XRF core-scanning. Those counter measurements will be used as a validation (testing) the calibration models.

2. LITERATURE REVIEW

2.1. MATSA Deposit in the Iberian Pyrite Belt

Iberian Pyrite Belt (IPB) has been one of the major mining districts in Europe since pre-historic times. It is an area of significant geological and metallogenic interest because it represents the largest concentration of metallic sulfide deposits on Earth (Leistel et al. 1997; Martin-Izard et al., 2015; Sánchez-España et al., 2000). With more than 2000 Mt of massive sulfide ore, the IPB hosts multiple world-class deposits such as Rio Tinto, Cobre las Cruces and Neves Corvo (Martin-Izard et al. 2015).

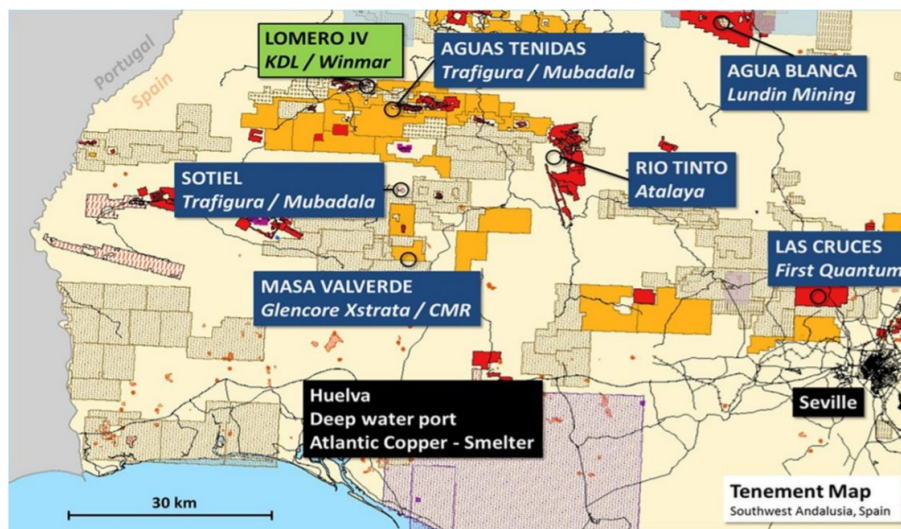


Figure 2. Iberian Pyrite Belt with its major high grade deposits and operations

The mines of Aguas Teñidas are located in southern Spain around 80 kilometers north of Huelva and 110 kilometers northwest of Sevilla (Figure 2). The current operator of mining operations is MATSA (Minas de Aguas Teñidas SAU). MATSA is Spanish company that was formed as a joint venture between Mubadala Development Company PJSC (based in the United Arab Emirates) and Trafigura Pte Ltd (based in Singapore) (MATSA, 2019)

The Aguas Teñidas mines dates back to 1930's. Followed by several closing and re-opening of the mine, operation commenced again in 2006 by the current owner MATSA. In addition to the Aguas Teñidas mines, MATSA holds the rights to the Magdalena mines in Almonaster La Real, and to the Sotiel Mine, which are located in the municipality of Calañas, Huelva. Magdalena deposit was discovered in 2011 a few kilometers from the Aguas Teñidas deposit and has started production in 2015. Tonnage of this deposit are lower compared to the neighboring mines, but it has higher metallic grades. The third operating mine is Sotiel, located 20 kilometers south of the other mines, also restarted in 2015. In addition to the operating mines, MATSA is running a number of exploration projects for new potential deposits (MATSA, 2019).

2.1.1. Geological Setting

The geology of IBP is a result of successive rifting, subduction zones and continental collisions which has followed the effects of plate tectonics and weathering processes in Western Europe throughout geological time. As shown on top right corner of Figure 3, The IPB was formed by a collision of continental blocks; the south Portuguese zone (SPZ), the Ossa Morena zone (OMZ) and the ensemble of the central Iberian zone (CIZ), the west Asturian-Leonese zone (WALZ) and the Cantabrian zone (CZ). Subsequently, the IPB was formed within the SPZ as a series of marine basins formed by transcurrent faulting during the early carboniferous age (Gumiel, 2010; Martin-Izard et al., 2015; Tornos, 2006).

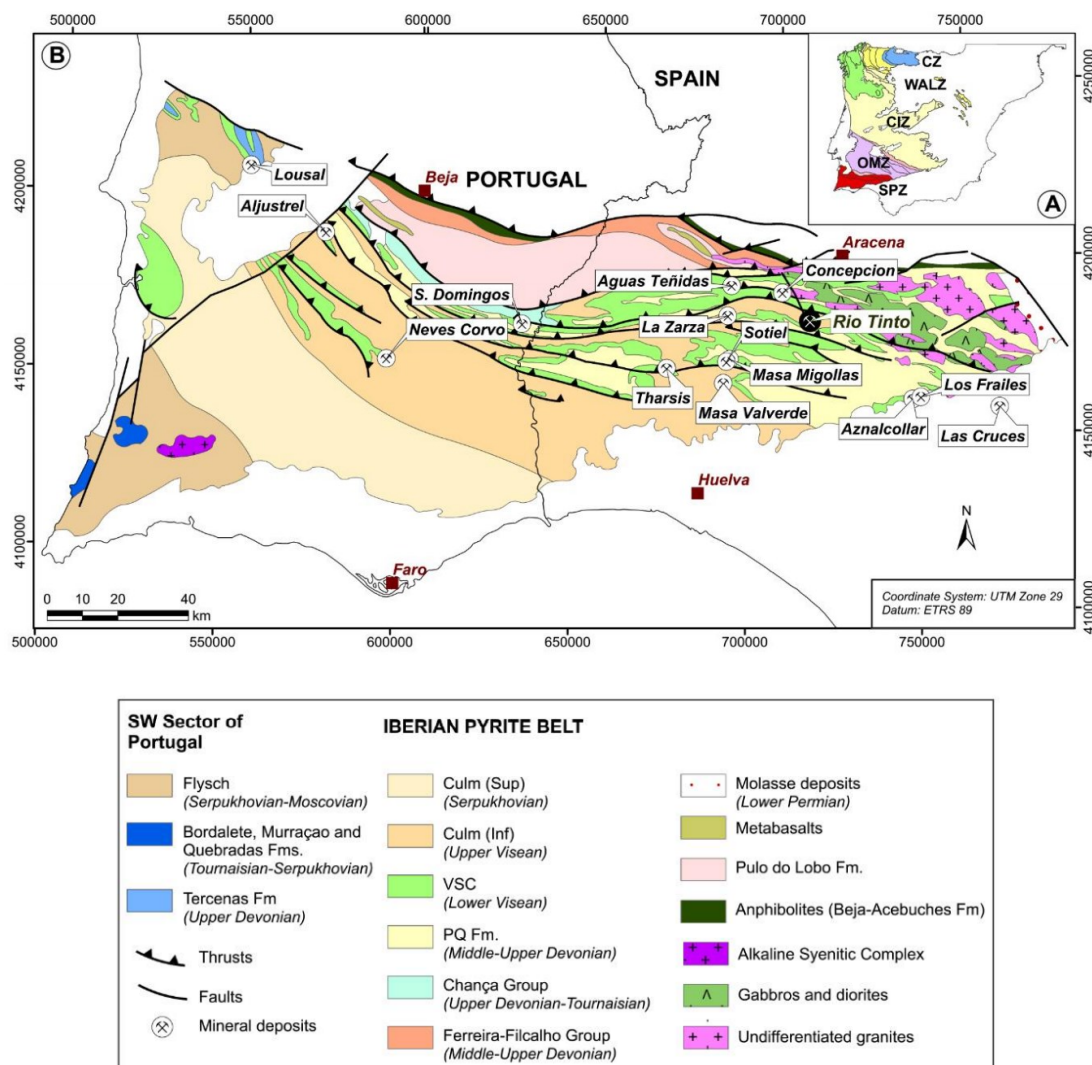


Figure 3. Geological setting of the IPB along with the different zones and major deposits (Martin-Izard et al., 2015).

Geodynamic interpretations suggest that the IPB was affected by extensional tectonic processes during the Late Devonian–Mississippian transtensional phase. Such regime was responsible for the breakdown and compartmentation of the basin and the onset of volcanism. This paleogeographic scenario favored the generation of anoxic sub-basins where massive sulfides accumulated. The episodic ascent of magma, just below the segmented basin, could have triggered the establishment of a hydrothermal system. Large volumes of seawater with connate water trapped in the volcanic and sedimentary pile may have been the source of the fluids necessary for the transport and disposition of metals. It is commonly accepted that massive sulfide deposits in the IPB were deposited between the late Famennian and early Visean (Martin-Izard et. al. 2016; Moreno et. al. 1996).

2.1.2. Regional Stratigraphy

Although establishing a litho-stratigraphic succession of the IPB is difficult because of its' complicated lateral facies variation and intense deformation (Leistel et al., 1997), an effort has been made to provide a simplified stratigraphic column. A simplified stratigraphic column for the IPB presented by Tornos (2006) consists very roughly of three units (Figure 4). The oldest units found in the area are grouped within a formation deemed the phyllite-Quartzite (PQ) group. This formation, formed by Late Devonian (Famennian), is a 1000 to 5000 meter thick sequences of alternating mudstones and sandstones originating from a continental platform.

Overlaying this PQ formation is the Volcano-Sedimentary Complex (VSC), which is from an economic perspective the most interesting formation as it hosts all deposits in the IPB. The VSC is a complex sequence of mafic and felsic volcanic layers with some interbedded mudstones dated back to the late Famennian to the early late Visean of age. Due to its volcanic nature, the complex is highly regionalized and varies strongly in thickness (ranging from 0 to 1300 meters) throughout the area. (Tornos, 2006). A turbiditic sequence of shales and litho-arenites tops the VSC group. This sequence is on average 3000 meters thick and is late Visean to middle-upper Pennsylvanian of age (Tornos, 2006).

AGE		LITHOSTRATIGRAPHY	
Quatern.		Sand and gravel	
Pliocene		Marls and argillaceous sediments	
Miocene		Limestones, sandstones and conglomerates	
CARBONIFEROUS	Culm Group	Slates with thick greywackes (gr) beds	
		Slates (partly carbonaceous) with greywacke (gr) lenses	
	Volcanic-sedimentary complex	VSC3	Submarine acid volcanics: Lavas, breccias, agglomerates. Massive felspar tuffs.
		Purple slates	
		VSC2	Massive sulfides ore bodies (VMS2) and carbonaceous black shales Tuffaceous slates, fine grained tuffs with cherts, argillaceous slates. Submarine acid volcanics: lavas, breccias, agglomerates and massive felspar tuffs
		VSC1	Submarine basic volcanics: Spilitic lavas and pyroclastics. Diabase sills. Purple slates with lenses of jaspers (Jp)
VSC0	Massive sulfide ore bodies (VMS1) in carbonaceous black slates and tuffaceous rocks. Black carbonaceous slates. Tuffaceous slates and cherty tuffs. Submarine andesitic volcanics: Lavas, breccias, agglomerates, massive felspar tuffs Argillaceous siliceous and tuffaceous slates		
UPPER DEVONIAN	Slate-quartzite Group (PQ)	Argillaceous and silty slates Quartzites and quartzitic conglomerates (qtz) Base unknown	

Figure 4. Simplified stratigraphic column of the IPB (Martin-Izard et al. 2016)

From economic geology point of view, the Volcano-Sedimentary Complex (VSC), is the most prominent sequence in the IPB. Several studies have tried to subdivide the VSC into subsections; VSC0, VSC1, VSC2 and VSC3 based on the mafic-felsic compositional divergences, structural features and depositional systems to identify favorable areas of mineral occurrence. Only VSC0 and VSC2 units are known to possibly host VMS deposits. (Arias et al. 2011; Leistel et al. 1997; F. Tornos et al. 2008).

Figure 4 shows a simplified stratigraphic column of the IPB presented by (Martin-Izard et al., 2016). It is a modified version of the stratigraphy constructed by (Straus & Gray, 1986). Based on the Martin-Izard (2016) stratigraphic column of the IPB, the sequence of the VSC from the bottom to top is as following:

- VSC0: Initial andesitic to felsic volcanism with interbedded black, tuffaceous and cherty slates hosting massive sulfides;
- VSC1: Basic (basaltic) rocks with intercalated black slates and conglomerates;

- VSC2: Acid volcanic (rhyolites and dacites) rocks;
- VSC3: Purple slates and acid volcanism.

The massive sulphides in IPB are hosted either by black shales or by acid volcanics whereas the basic rocks are considered barren when not cut by stockwork mineralizations

2.1.3. Iberian Pyrite Belt Genesis Model

The depositional environment of the massive sulphides in the IPB has been a subject of study for several decades and thus several hypotheses have been developed. The most recent ore genesis models are proposed by Tornos (2006) and Martin Izard et al. (2016). Both studies basically defined two types of metal formation processes in the IBP which differs according to its geographic position (Figure 5):

1. Exhalative ores: the first type of deposits are exhalative ores formed on the bottom of a brine pool mostly hosted by shales and concentrated in the southern portion of the belt in half-graben basins. They are formed by the precipitation of metals from the upwelling of deep, sulphur-depleted fluids mixed with biogenetic sulphur-rich seawaters. Characteristics of these VMS are large, stratiform orebodies with low metal grades. These VMS deposits are mostly confined to the southern part of the IPB (Tornos, 2006).
2. Replacement-style mineralization: the second type of deposit is interpreted as a replacement-style mineralization within graben structures and pull-apart basins primarily hosted by massive or volcanoclastic, felsic-rich rocks (Martin-Izard et al., 2016). The formation is interpreted as replacement of porous or reactive volcanic rocks by precipitation of ore due to mixing of deep fluids with modified seawater (Tornos, 2006).

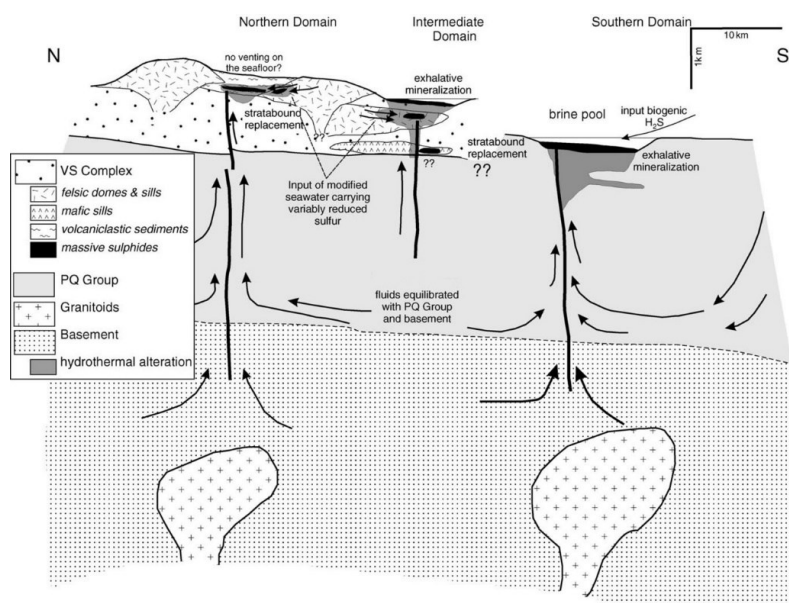


Figure 5. Two mineralization systems in the IPB (Tornos, 2006).

2.1.4. Metallogeny

The deposits of the IPB consist of different morphologies; mainly massive sulfides, stockworks, stratiform and disseminated. But, the mineralizations of most deposits are similar consisting primarily of pyrite, chalcopyrite, sphalerite and galena with accessory occurrences of tetrahedrite tennantite, cassiterite and pyrrhotite (Leistel et al., 1997). The mineralization style is dominated by sphalerite and galena, and chalcopyrite. As shown on the microscope images in Figure 6, these minerals partially replace and fill open spaces in pyritic orebodies. Sphalerite and galena can occur either isolated or forming intergrowth and galena filling interstices in sphalerite (Almodóvar et. al. 2019).

Most mining and exploration operations in the IBP focus on the extraction of Cu, Pb and Zn. In addition to Cu, Pb, Zn and Fe, considerable concentrations of Sn, Bi, Co, Te, Se, Au and Ag have also been identified along with some non-economical mineralizations of Mn and W in the Volcano-Sedimentary Complex (VSC) (Leistel et al. 1997).

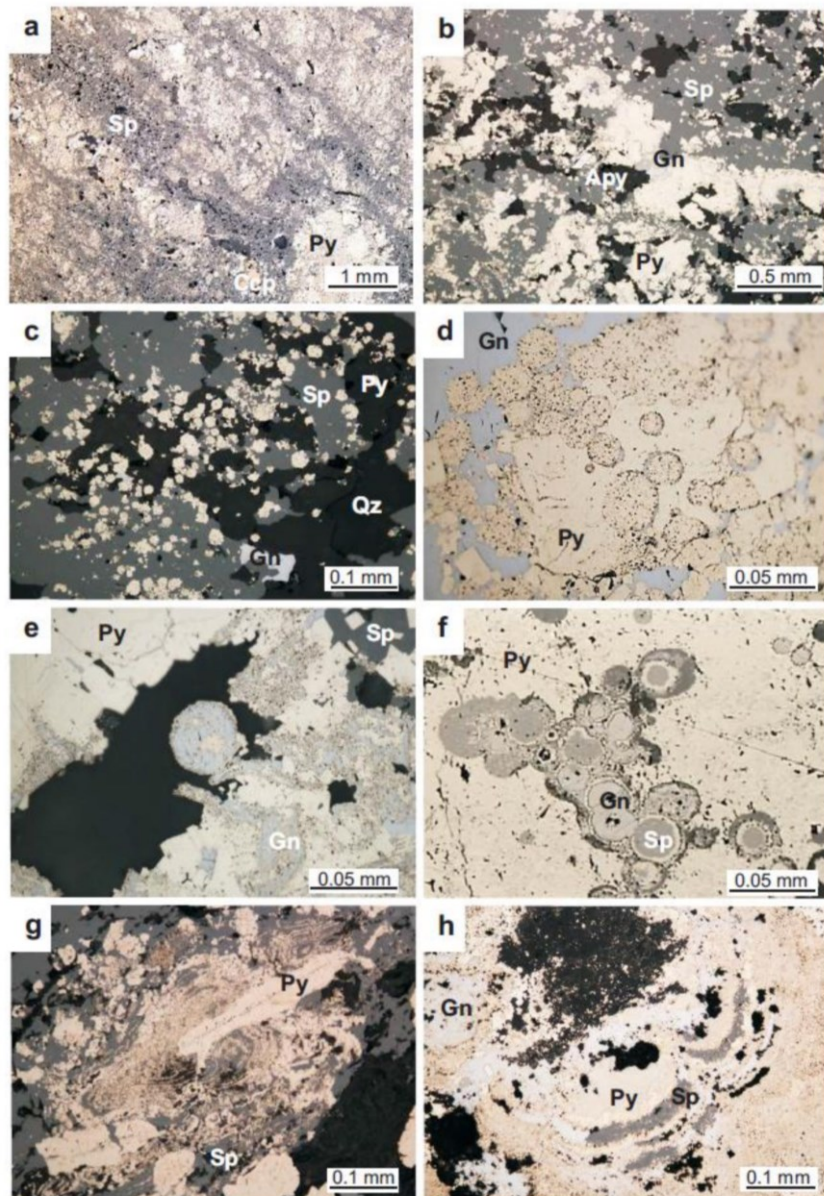


Figure 6. Optical microscope images of polymetallic mineralizations from several massive sulfide deposits of the Iberian Pyrite Belt (Almodóvar et. al. 2019).

2.1.5. MATSA Mining and Mineral Processing Operations

As mentioned earlier, the mining activities of MATSA consist of three operating mines; namely Aguas Teñidas, Magdalena and Sotiel. Discovered in 1980, Aguas Teñidas is the largest mine among the three projects. The mining rights have shifted several times from one company to another in the 20th century. Due to crisis in the mining sector, production stopped in 2001 but 5 years later the project commenced again. The Magdalena mine is located just few kilometres east of Aguas Teñidas. The deposit was discovered in 2011 and production started 4 years later. Despite the lower volume, this deposit is composed of the highest grades in the area. The Sotiel deposit, located approximately

20 km south from Aguas Teñidas and Magdalena, restarted production in 2015 after being closed for 15 years (Beare et. al. 2006; MATSA 2016)

All three mines utilize the same longhole stoping method, working from bottom to top in primary and secondary stages. Aguas Teñidas and Magdalena use tailings for backfilling that allows for almost complete extraction of the orebodies where tailings are dried and transformed into an inert paste and backfilled to the voids after the stopes are mined out (MATSA, 2017).

All the three mines produce two different types of ores; cupriferous ores, and the more valuable polymetallic ores. Processing of ore from all three mines is done in one processing facility located at the Aguas Teñidas facility. As shown in Figure 7, the processing of both ore types has been entirely separated into two different lines for the following reasons (SRK consulting, 2006):

- The two mineralization types have very distinct grades and are separated by well-defined geological boundaries;
- Early stage metallurgical testing indicated that the optimum grind for copper ores was much coarser than the polymetallic ores.
- Recovering copper concentrate from blended ores with satisfactory grade was found to be problematic, while copper was easily floated from the cupriferous ore;
- Consistent blending requires extra challenges in the logistics of the mining operation

The beneficiation process is depicted in flowsheet below (Figure 7). The comminution stage consists of a primary SAG stage with secondary ball mills and tertiary vertical mill using ceramic beads. After milling to optimum particle size, the ores are concentrated using flotation, creating copper concentrate, zinc concentrate and a relatively minor amount of lead concentrate (MATSA, 2017).

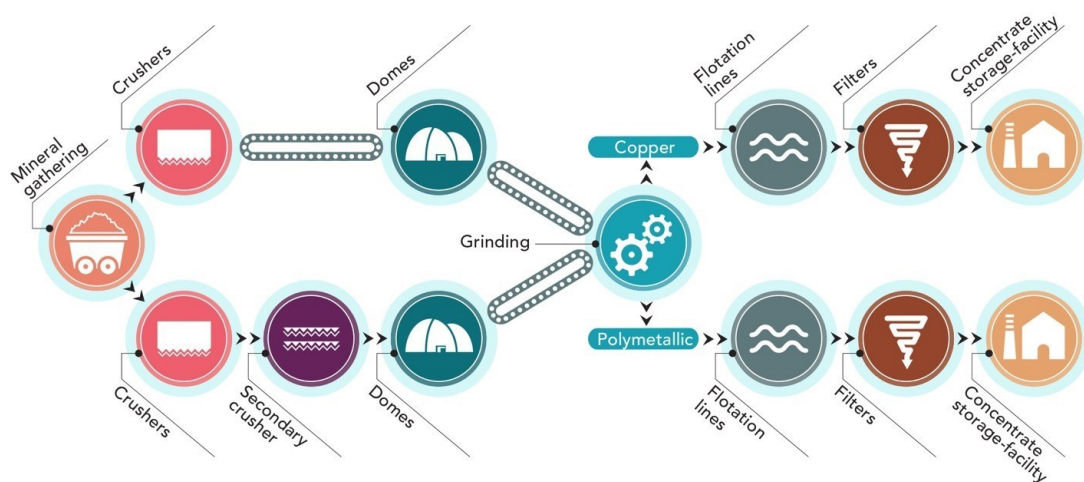


Figure 7. Simplified mineral processing flowsheet (MATSA, 2016).

2.2. X-Ray Fluorescence (XRF)

2.2.1. Historical and Scientific Background

X-rays were discovered by Wilhelm Röntgen at the University of Würzburg in Germany in 1895. While performing experiments with cathode ray tubes, which accelerate electrons towards an anode target, Röntgen discovered that the tubes produced invisible rays of light that were able to penetrate a layer of thick black cardboard and cause a fluorescent effect on a screen painted with barium platinocyanide. As the nature of this radiation was still unknown, Röntgen used the term “x-rays”, which is still in use today. Later, other physicists were able to measure the properties of these rays, such as polarization, diffraction, refraction and reflection, which firmly established that they were a form of electromagnetic radiation. However, the development of x-ray fluorescence spectroscopy required further advances in quantum physics (R Scholtz et. al. 2006; Beckhoff et. al. 2007, Van Grieken et. al. 2001).

The photoelectric effect was first observed by Alexandre Becquerel in 1839. Electrons can be emitted when radiation hits a material, which according to classical electromagnetic theory, occurs due to energy transfer from the radiation to the electrons. However, in empirical studies, electrons are only emitted when the energy of the radiation exceeds a threshold value referred to as the “work function”. This phenomenon was not adequately explained until Albert Einstein described light not as a continuous wave but rather as a photon, or a packet with a defined energy. Electrons too are limited to discrete energy levels, or quantum states, when bound in an atom. The “work function” is simply the difference in energy between the bound and free electron states that must be exceeded for electron emission to take place. After the electron is ejected, internal relaxations of bound electrons from one quantum state to another cause emission of x-rays with energies characteristic of the irradiated atom. Detection of these x-rays is the backbone of x-ray fluorescence spectroscopy (R Scholtz et. al. 2006; Beckhoff et. al. 2007, Van Grieken et. al. 2001).

According to Einstein’s theory, when electrons are bound to an atom, they must occupy one of many discrete energy states. The probability of transitions between these states are governed by selection rules derived in subsequent studies: the most likely transitions are termed electric dipole allowed electronic transitions and produce the most visible peaks in an XRF spectrum. Figure 9 shows a typical energy level diagram as well as the accompanying transitions most relevant to XRF.

2.2.2. Fundamentals of X-Ray Fluorescence

From a physical point of view, X-rays are of the same nature as visible light. Visible light can be described as electromagnetic wave radiation whose variety of colors (e.g. the colors of the rainbow) we interpret as different wavelengths. The wavelengths of electromagnetic radiation reach from the kilometer range of radio waves up to the picometer range (10^{-12} m) of gamma radiation (Figure 8).

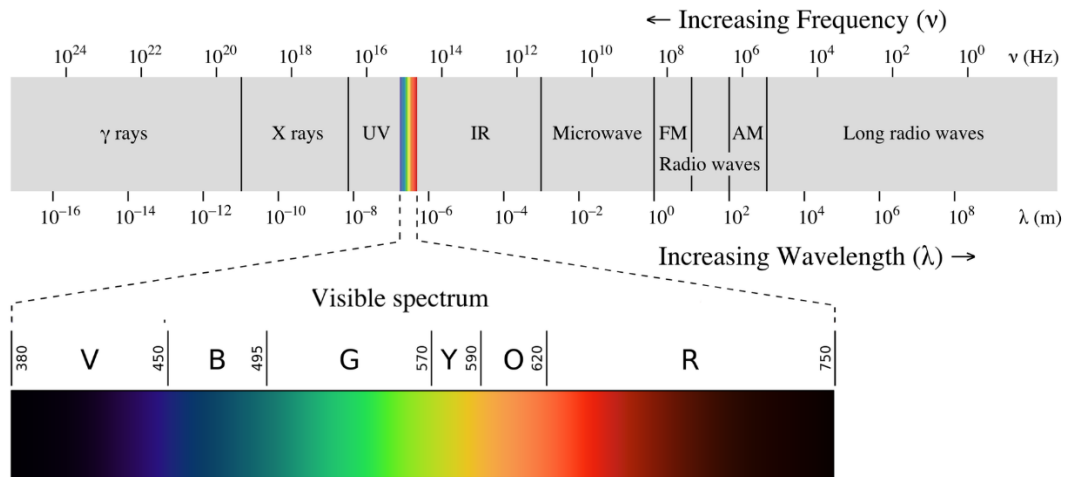


Figure 8. The electromagnetic spectrum (Wikipedia, 2021)

X-ray fluorescence is a physical phenomenon corresponding to the emission of characteristic “secondary” X-rays from a material that has been excited by bombarding it with high energy X-rays or γ -rays. X-rays belong to the portion of electromagnetic waves with wavelengths in the range of 0.02 to 11.3 nanometers. This corresponds to frequencies in the range 30 petahertz to 30 exahertz (3×10^{16} Hz to 3×10^{19} Hz). They are shorter in wavelength than ultraviolet rays (UV) and longer than gamma rays (R Jenkins et. al. 1981).

Given wavelength of X-rays; $\lambda = 0.02 - 11.3$ nm

According to Planck’s equation: $E = \frac{h c}{\lambda}$

Where $c = 3.00 \times 10^8$ m/sec and $h = 6.63 \times 10^{-34}$ J sec

Therefore; XRF analysis covers the following range of energy or wavelengths:

- $E = 0.11 - 60$ keV
- $\lambda = 0.02 - 11.3$ nm

In addition to the wave properties, light also has the properties of particles (called “Dual nature of light”). This is expressed by the term “photon”. In this paper, the term “quanta” or “X-ray quanta” is used for the same purpose.

2.2.3. X-Ray Fluorescence in Atoms

Bohr's atomic model describes the structure of an atom as an atomic nucleus surrounded by electron shells. The positively charged nucleus is surrounded by electrons that move within defined areas ("shells"). The individual shells are labeled with the letters K, L, M, N etc. The innermost shell being the K-shell, the second innermost the L-shell etc. The K-shell is occupied by 2 electrons. The L-shell has three sub-levels and can contain up to 8 electrons. The M-shell has five sub-levels and can contain up to 18 electrons (R Scholtz et. al. 2006; R Jenkins, 1999; Bruker, 2006).

The differences in the strength of the electrons' bonds to the atomic nucleus are very clear depending level they occupy, i.e. they vary in their energy. This is referred to as "energy levels" or "energy shells". To release an electron of the second innermost shell from the atom, a clearly defined minimum amount of energy is required that is lower than that needed to release an innermost electron. (R Scholtz et. al. 2006; R Jenkins, 1999; Bruker, 2006). The minimum amount of energy required to release an electron from the atom is referred to as the "binding energy" of the electron in the atom. (Note: energy level = binding energy)

When excited by the primary high energy X-rays, electrons are ejected from the sample atoms. When electrons from inner orbitals are ejected they leave holes that are to be filled by electrons from the outer orbitals. As electrons fall down from the outer orbitals to the inner orbitals, new X-rays are generated at energy difference between the two orbitals as shown on Figure 9. These secondary emissions are called "X-ray fluorescence". Each element has its specific X-ray fluorescence emissions which correspond to specific energy differences between orbitals. Thus, every fluoresced X-Ray is part of the XRF signature of a specific element (R Scholtz et. al. 2006; R Jenkins, 1999).

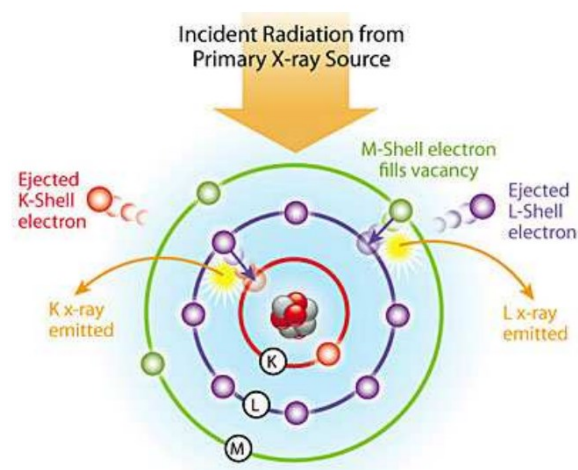


Figure 9. Generating X-Ray Fluorescence in an atom (Niton, 2021)

K-radiation is the term given to the radiation released when replenishing the K-shell, L-radiation to that released when replenishing the L-shell etc. (Figure 10). Also needed for the full labeling of the emitted X-ray line is the information telling us which shell the electron filling the “hole” comes from. The Greek letters α , β , γ , are used for this with the numbering 1, 2, 3, to differentiate between the various shells and sub-levels.

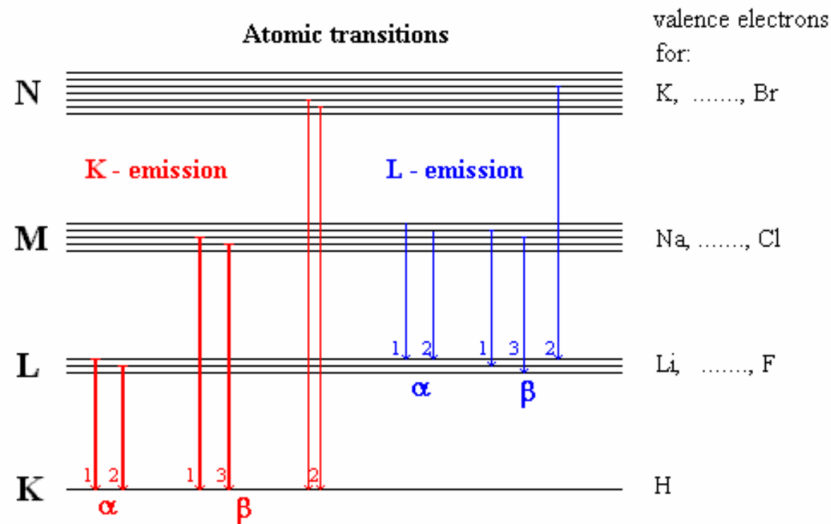


Figure 10. X-Ray radiations labeling

Examples:

- $K\alpha_1$ = Electron from sub-level L_{III} to the K-shell
- $K\alpha_2$ = Electron from sublevel L_{II} to the K-shell
- $K\alpha_{1,2}$ = if neither line is resolved by the spectrometer
- $K\beta_1$ = Electron from sublevel M to the K-shell
- $L\alpha_1$ = Electron from sublevel M to the L-shell

2.2.4. X-Ray Tube (Generation of X-Rays)

The purpose of X-ray fluorescence is to determine chemical elements both qualitatively and quantitatively by measuring their characteristic radiation of the elements present in the sample. To do this, a method must be applied that is suitable for releasing electrons from the innermost shell of the chemical element in a sample. This involves adding to the inner electrons amounts of energy that are higher than the energy bonding them to the atom. Incident/primary high energy X-rays proves to be the technically most straightforward and, from the point of view of radiation protection, the safest solution to eject electrons from the sample atoms Incident/primary high energy X-rays are almost always generated using an x-ray tube. An x-ray tube functions as a specific energy converter, receiving electrical energy and converting it into two other forms of energy: x-ray radiation (1%)

and heat (99%). Heat is undesirable product of this conversion process (Reinhold et. al. 2000; Rene et. al. 1992; Bruker, 2006).

As shown in Figure 11, a typical X-ray tube has the following basic components:

- *Cathode Filament*: is negatively charged material that produces electrons through thermionic emission. Filaments are often made of thoriated tungsten. Because tungsten provides higher thermionic emission than other metals.
- *High voltage field*: is a high voltage supply between the cathode and anode (target). It accelerates the electrons toward the anode (target) material.
- *Vacuum chamber*: as air molecules can block and obstruct the path of the electrons, this component serves to avoid such obstructions. Thus, it helps the electrons to reach the anode with high kinetic energy.
- *Anode/target material*: is a positively charged side of the X-ray tube. It converts electron's kinetic energy to X-ray photons when the accelerated electrons collide with it. Thus, the electrons are decelerated (retarded) enormously. When the electrons from cathode interact with anode, more than 99% of their kinetic energy is converted into heat. As this heat must be dissipated quickly, the anode must be a good heat dissipator. Additional cooling component maybe also used to avoid overheating the X-ray tube. Most common materials used as anode are molybdenum, tungsten, rhodium and copper. Different anode materials generate different X-ray spectrum.
- *Lead shielding*: electrons and X-ray photons are harmful to human body and thus operator need protection from scattered radiation. This component is used to contain stray electrons and X-ray photons from flowing freely out of the X-ray tube. Because lead has great ability to absorb radiation because it has larger nucleus (higher density cloud), it is used as shielding component.
- *Filter*: is a thin sheet of aluminum that absorbs low energy photons and let high energy photons pass through the exit window into the sample. Thus, it enhances the signal-to-noise ratio by reducing interferences and background.
- *Exit window*: is made from very light elements such as beryllium.
- *Collimator*: is an aperture that controls the spatial resolution of the incident XRF.

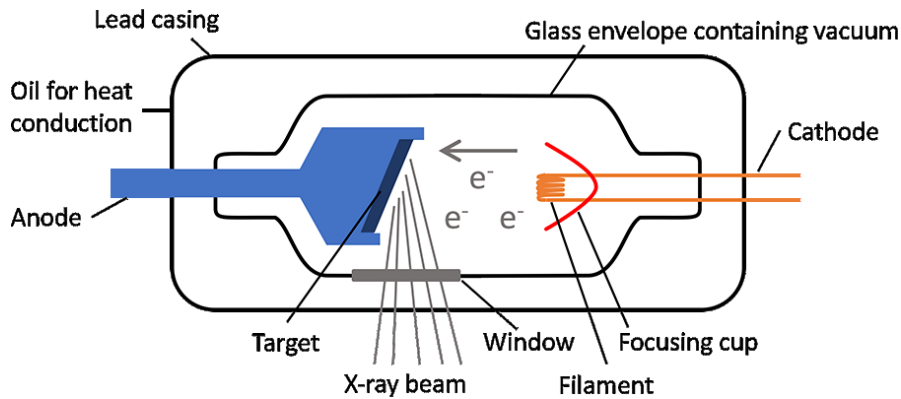


Figure 11. X-Ray Tube components

When operating the X-ray tube, the tube current (mA) and voltage are used to control the desired incident X-ray spectrum:

- *The X-ray tube current (mA):* increasing the current of the cathode filament increases the number of electrons produced in the cathode. Increasing the number of electrons accelerated toward the anode means a direct increase in the number of incident X-ray photons produced by the X-ray tube. This is related to the concept of spectrum intensity in CPS (counts per second) (i.e. y-axis in XRF spectrum as shown in Figure 12).
- *The X-ray tube potential/voltage (KV):* the potential difference applied to the x-ray accelerates the electrons from cathode to anode. Increasing the potential difference/voltage (KV) increases the kinetic energy of the electrons and thus directly increases the energy of the X-ray photons generated (i.e. x-axis in XRF spectrum as shown in Figure 12).

2.2.5. Bremspektrum (Continuum) and Characteristic Radiation of Anode Material

The proportion of the electron energy loss emitted in the form of an X-ray can be between zero and the maximum energy that the electron has acquired as a result of the acceleration in the electrical field. For example if 30 kV (kilovolt) are applied between the anode and cathode, an electron acquires 30 keV (kilo-electron-volts) energy from passing through this voltage. (Note 1 eV is the energy that an electron acquires when passing through a potential of 1 Volt). Thus, an X-ray photon with maximum energy of 30 keV can be acquired from deceleration in the anode material, i.e. the distribution of the energies of numerous X-rays is between zero and 30 keV (Reinhold et. al. 2000; Rene et. al. 1992; Bruker, 2006).

Figure 12 shows a typical X-ray tube spectrum profile generated by accelerating 0.5 mA electron current toward a molybdenum anode/target with 30 kV accelerating voltage. The spectrum can be divided into two components: Bremspektrum (continuum) and characteristic radiation of anode material;

- *The Bremspektrum (continuous spectrum)* is generated by electrostatic deceleration of the electrons by nuclei in the anode target (Molybdenum in this case). As the electrons lose kinetic energy, this energy is released in the form of x-ray radiation, which is continuous because it is generated from free electrons. The highest-energy bremsstrahlung is generated due to complete deceleration of electrons and is directly proportional to the acceleration voltage in the tube. In Figure 12, the electrons are accelerated by a voltage of 30 kV, which corresponds to a maximum x-ray photon energy of 30 keV.
- *Characteristic peaks of anode material*, on the other hand, are generated as a result of electron transitions within the atoms in the metallic anode target. When an accelerated electron comes into contact with an atom in the target, there is a possibility that its energy will be transferred to one or more of the atom's bound electrons, which is ejected as a photoelectron. The excited atom then has a vacancy in one of its energy shells (Figure 9) that can be filled by the relaxation of an electron in a higher-energy shell and the subsequent emission of characteristic radiation. Characteristic peaks of anode material are of major importance for X-ray fluorescence analysis. This characteristic radiation appears as peaks in the emission profile of the x-ray tube (Figure 12) and in the measured spectrum of the sample

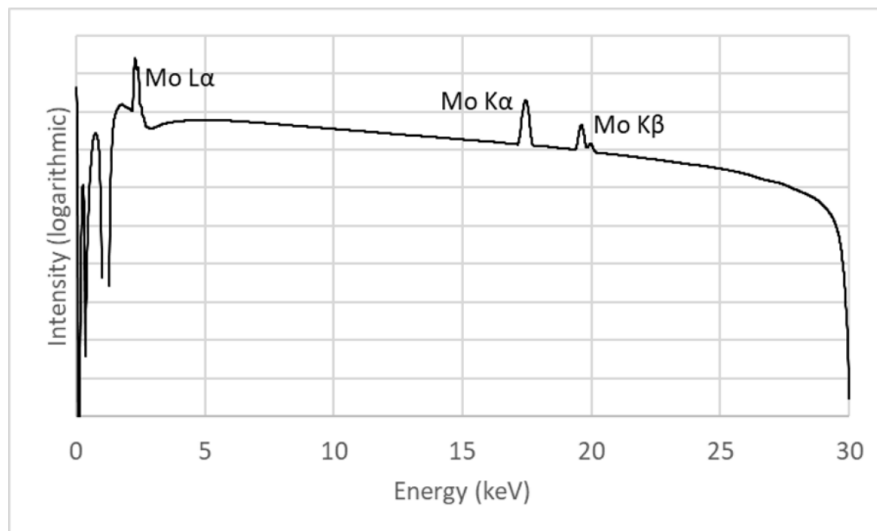


Figure 12. Spectrum emitted by a Mo x-ray tube with 30 kV accelerating voltage and 0.5 mA electron current (Bruker, 2016)

After interaction with the sample material, all the x-ray photons are then detected by the detector of the XRF instrument and processed to display a spectrum. XRF spectra represent intensities (counts of X-rays) versus energies or wavelengths.

2.2.6. Interactions of Incident X-Rays with Sample Material

Once the incident x-ray photons are produced in the x-ray tube, they are directed toward the sample. The purpose of X-Ray fluorescence is the qualitative and quantitative determination of elements in a sample by measuring characteristic radiations. Yet, in addition to the fluorescence process, X-Rays can be scattered, absorbed or transmitted by the material as shown on Figure 13 (R Scholtz et. al. 2006). This scattering can occur both with and without loss of energy (Compton and Rayleigh scatterings).

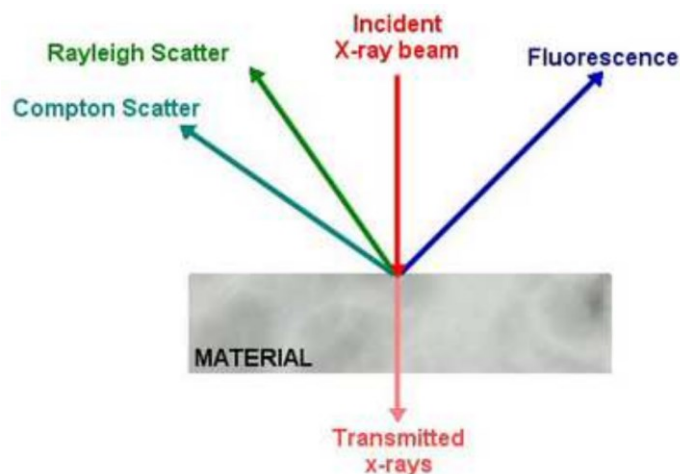


Figure 13. Different types of secondary X-rays emissions; fluorescence, transmission and scatterings (R Scholtz et. al. 2006)

The x-ray-sample interaction can be explained at atomic level (Figure 14). Considering the particle-like properties of x-ray radiation, the photon, penetrating through a sample, can engage with the electrons of the atoms. Depending on how the photon energy E_o corresponds to the encountered electron's binding energy E_{Be} , the incident photon can produce one or more of the following phenomenon: (R Scholtz et. al. 2006; Rene et. al. 1992; Bruker, 2006).

- *Transmitted* (no interaction with the atom)
- *Absorbed* (photoelectric absorption, $E_o \approx E_{Be}$): passing through matter weakens the intensity of x-rays. The degree of this weakening depends on both the radiation energy and the chemical composition of the sample. Heavier elements absorb better than light ones. E.g. 1 mm of lead absorbs practically all of the higher-energy radiation occurring during X-ray fluorescence, whereas 1 mm of polypropylene is more or less permeable to x-rays. Low-energy X-ray quanta are absorbed more readily than quanta with higher energy.
- *Characteristic X-ray (Fluorescence)*: as inner e- are ejected and e- fall down from the outer to the inner orbitals, new secondary emissions, called "X-ray fluorescence" is generated. This radiation is of major importance for XRF analysis.

- *Rayleigh scattering* (elastic, without loss of energy, $E_o > E_{Be}$): the photon coming from the tube scatter in the sample material without losing energy and can thus enter the detector and be measured. These peaks appear as “peaks of the anode material” (e.g. rhodium) in the spectrum (Figure 16).
- *Compton scattering* (inelastic, with loss of energy, $E_o > E_{Be}$): the photon coming from the tube strike the sample element’s e-. So some of a photon’s energy is transferred to the e- (called “compton electron”). Since the x-ray quantum loses energy, it is scattered with less energy and such peak appears on the low-energy side of the spectrum after detection. These peaks are called “Compton peaks” (Figure 16).

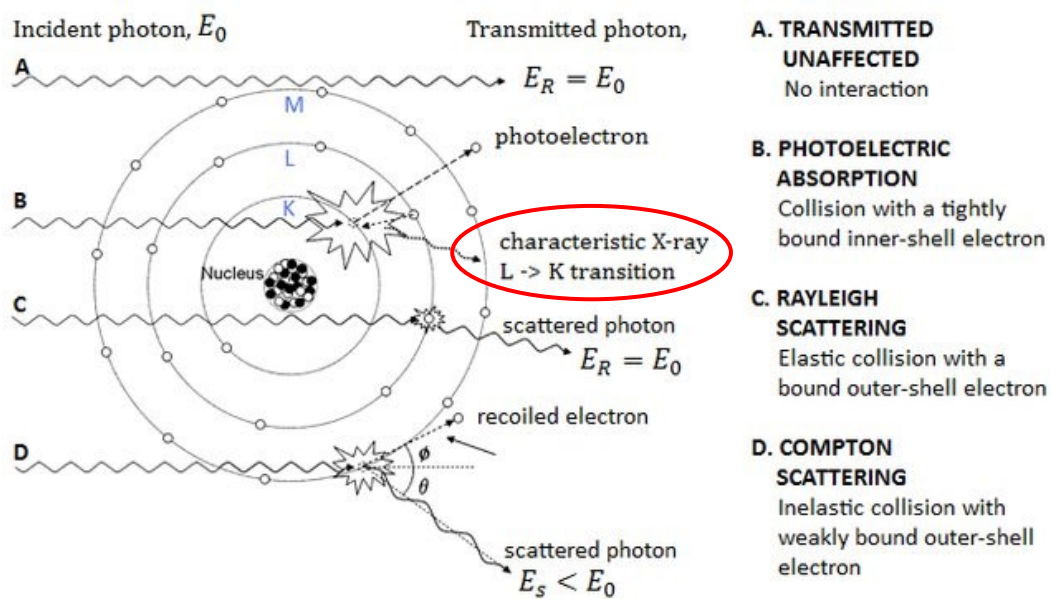


Figure 14. Types of Interactions between an X-ray photon and the atom of irradiated matter for x-ray beam energy (Seibert J.A and Boone J.M., 2005)

2.2.7. Detection of X-Rays

Like other spectroscopic techniques, XRF instruments rely on the generation of an electrical signal in response to the impact of a generated photon on a detection device. The fluorescent X-rays emitted by the material sample are directed into a solid-state detector which produces a "continuous" distribution of pulses, the voltages of which are proportional to the incoming photon energies (Figure 15). This signal is processed by a multichannel analyzer (MCA) which produces an accumulating digital spectrum that can be processed to obtain analytical data (Bruker, 2006).

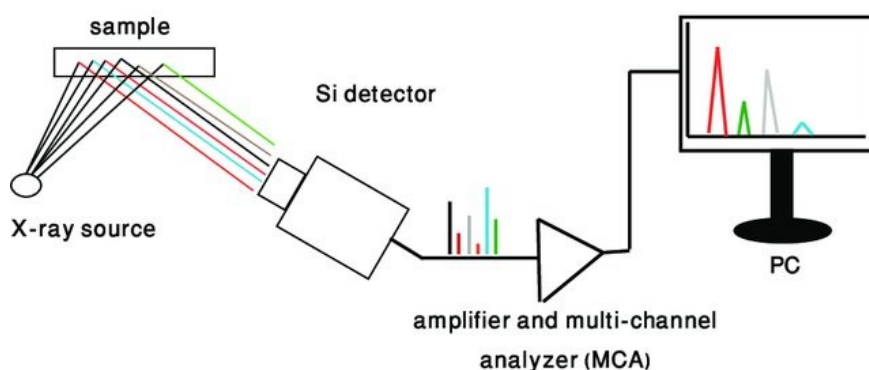


Figure 15. Basic components of Energy-Dispersive XRF

In order to differentiate between photon energies, the detector must consist of a semiconductor material. Through an x-ray absorption interaction - similar to that in the sample itself - the incident photon creates a “cloud” of photoelectrons and electron holes in the semi-conductor. These charge carriers are separated by an applied voltage and thus generate a measurable voltage pulse, which is amplified, processed and classified by the detector electronics in channels.

The strength of the pulse is directly proportional to the energy of the photon. Energy-dependent spectra such as that in Figure 16 are generated by classifying the detected photons into one of a series of evenly-spaced “channels” and plotting the number of detected photons (“counts”) against the channel number (energy).

There are a variety of detector options, each with its own advantages and disadvantages. For many years, the Si (Li) detector has been the standard in detection technology. It is based on the architecture of a PIN diode. The main disadvantage of Si (Li) detectors is the need to cool with liquid nitrogen to keep noise low. A more modern variant of the semiconductor detector called the silicon drift detector (SDD) is most commonly used detector nowadays. It consist of a high-purity silicon crystal with a very low leakage current, which significantly reduces noise and requires only a small amount of cooling, which can be achieved with a small peltier cooler. Other advantages of SDDs include significantly higher count rates, smaller size and lower manufacturing costs compared to Si (Li) detectors (Reinhold et. al. 2000; Bruker, 2016).

In principle, however, both silicon-based detector types reach their limits if the photons to be detected are very fast, i.e. have high amount of energy (> 40 keV). Silicon is a light element and cannot absorb a significant fraction of these high-energy photons, which drastically reduces the efficiency of SDD and Si (Li) detectors. For such applications, detectors with heavier elements such as a CdTe detector must be used as an alternative, but this entails considerable losses in energy resolution (Reinhold et. al. 2000; Bruker, 2016).

2.2.8. Interpretation of XRF Spectra and Classical Analysis

The purpose of X-ray fluorescence spectrometry is the qualitative and quantitative determination of the elements in a sample by measuring their characteristic radiation. As the sample is exposed to a beam of X-ray quanta from a tube, a proportion of these X-rays also reach the detector in the form of radiation background as a result of physical scattering processes. While the scattered Bremsstrahlung proportion generally produces a continuous background, the scattered characteristic radiation of the anode material contributes towards the peak/line spectrum.

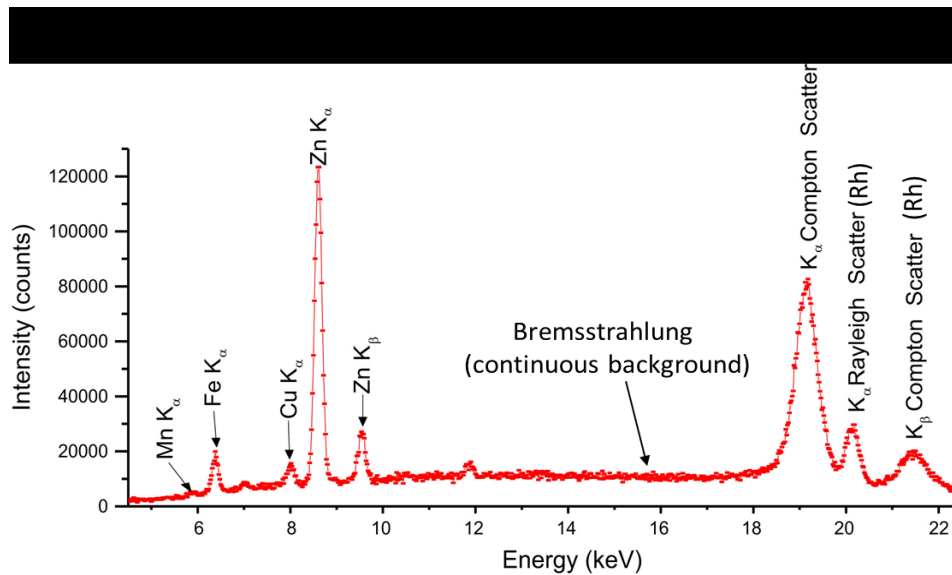


Figure 16. Typical spectrum of certified reference material (Mahuteau, 2008)

Prior to background correction and artifacts removal, a typical XRF spectrum consists of:

- *Characteristic XRF peaks of elements* from the sample (E.g. Mn-K α , Fe-K α , Cu-K α , Zn-K α and Zn-K β in Figure 16). The energy (KeV) of peaks in the spectrum correspond to the elements in the sample. Each element emits a unique spectrum of x-rays characteristic of that element with characteristic photon energy (qualitative elemental analysis). As shown in Figure 16, Cu has a weak K α peak at 8.05 keV while Zn has a strong K α peak at 8.64 keV. The number of x-rays (intensity/counts per second) in each peak is proportional to the number of atoms (quantitative elemental analysis). Analysis software detects which peaks are present finds the intensity of each peak and computes the concentration of each element in the sample.
- *Artifacts arising from X-ray tube source:* electrons with high kinetic energy (typically 10-50 kV) strike atoms in the X-ray tube anode/target material and transfer energy. The interaction of x-ray source photons with the sample generates several artifact features in the XRF spectrum which may include the following:

- Bremsstrahlung/ Bremsspektrum: due to backscattering of X-rays from sample to detector and appears as continuous background or very broad peak.
- Rayleigh peaks: peaks arising from target anode in X-ray tube source (Rhodium in this case). No energy is lost (elastic scattering) in this process so peaks show up exactly at characteristic x-ray energies (Rh-K α at 20.22 KeV in this case)
- Compton peaks: peaks arising from target element in X-ray tube. Some energy is lost in this process so peaks show up at energies slightly less than characteristic X-ray tube target energies (Figure 16 shows the Rh-K α -compton peak)
- *Artifacts arising from detection process:* the interaction of X-ray fluorescence photons from the sample with the detector can generate several different types of artifact peaks in an XRF spectrum which may include the following:
 - Sum peaks: are artifact peaks due to the arrival of 2 photons at the detector at exactly the same time. Figure 17 illustrates such peak when two Fe-K α photons with each 6.4 KeV are detected to form a combined sum peak of 12.8 KeV. It occurs in XRF spectra that have high concentrations of an element. It can be reduced by keeping count rates low.
 - Escape peaks: are artifact peaks due to the absorption of some of the energy of a photon by silicon atoms in the detector. Figure 17 illustrates such peak when Fe-K α photon loses 1.74 KeV to Si atom and thus producing an escape peak of Fe at 4.66 KeV. It is more prominent in XRF spectra that have high concentrations of an element and for lower Z elements. It can be reduced by keeping count rates low.

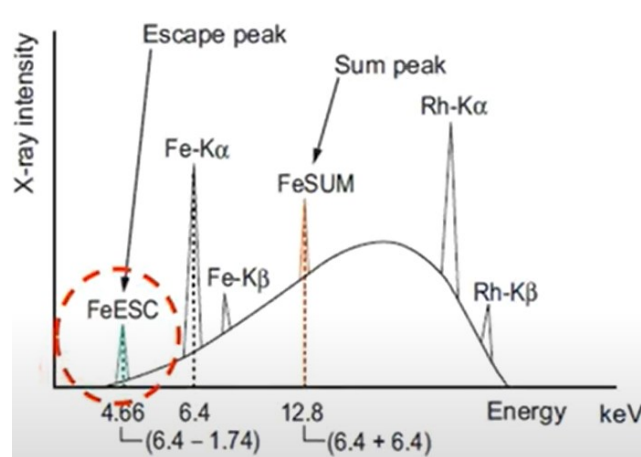


Figure 17. Sum and escape peaks in XRF spectrum

2.2.9. Extracting XRF Analytical Results and Matrix Effect

XRF provides qualitative data, i.e. identifying which elements are present in a sample by looking at their X-ray peak lines in the spectrum, and quantitative data (elemental composition) which is directly proportional to the number of x-ray photons detected (count rate). Extracting the qualitative elemental analysis from XRF spectra is straight forward process as far as the artifacts and noise are properly identified and removed. Whereas, quantitative analysis involves number of algorithms and calibration efforts.

At first sight, the translation of x-ray photon count-rates (intensity of peaks) into elemental concentrations would appear to be straightforward because Energy-Dispersive XRF (ED-XRF) separates the X-ray lines efficiently, and the rate of generation of x-ray photons is proportional to the element concentration. However, the number of photons leaving the sample is also affected by the physical properties of the sample: so-called "Matrix Effects" (G. J. Weltje et. al. 2008; Gullayanon, 2011; A. Buhler, 1998). These fall broadly into three categories:

1. *X-ray Absorption*: As discussed earlier, although all elements absorb x-rays to some extent, heavier elements generally absorb x-rays more than light ones. For example, the mass absorption coefficient of silicon at the wavelength of the aluminum $K\alpha$ line is $50 \text{ m}^2/\text{kg}$, whereas that of iron is $377 \text{ m}^2/\text{kg}$. This means that a given concentration of aluminum in a matrix of iron gives only one seventh of the count rate compared with the same concentration of aluminum in a silicon matrix. Fortunately, mass absorption coefficients are well known and can be calculated. However, to calculate the absorption for a multi-element sample, the composition must be known.
2. *X-ray Enhancement*: enhancement occurs where the secondary x-rays emitted by a heavier element are sufficiently energetic to stimulate additional secondary emission from a lighter element. Shown in Figure 18, a Si- $K\alpha$ x-ray photon is produced in a sample by the effect of an x-ray incident radiation. Inside the sample, it can be absorbed again by transferring its energy to an Al-K electron. This can then emit an X-ray quantum itself. The silicon radiation thus contributes to the X-ray emission of the aluminum. This is referred to as "secondary enhancement". In this particular example, aluminum count-rate is enhanced by the presence of silicon whereas silicon count-rate is underestimated (absorbed). In quantitative analyses, the effects of absorption and secondary have to be corrected. These phenomenon can be modelled mathematically and corrections can be made provided that the full matrix composition can be known.

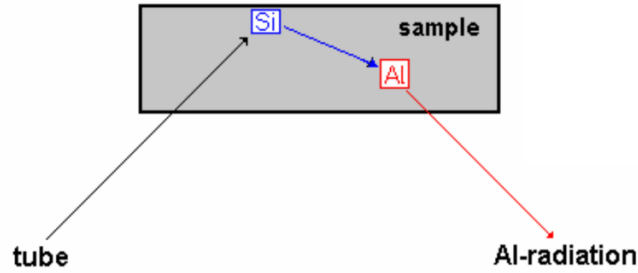


Figure 18. Secondary enhancement of aluminum by silicon atoms (Bruker, 2006)

3. *Sample Macroscopic Effects:* includes particle size effects, uniformity, inhomogeneity of the sample, and unrepresentative condition of the surface. In ideal world, Samples are homogeneous and isotropic, but they often deviate from this ideal condition. Considerable effort are required to minimize these effects. Because they are artifacts of the method of sample preparation, these effects cannot be compensated by theoretical corrections, and one way to reduce such effects is applying proper sample preparation.

2.2.10. Sample Preparation for XRF Analysis

XRF can analyze almost any material you can present to the spectrometer, but the better a sample is prepared, the more accurate the analytical results. As shown in Figure 19, the choice of sample preparation is always a balance between the quality of results required, the effort expend (labor, complexity) and the cost (sample preparation equipment, labor, time to analysis). The choice of method may be different for different materials depending on the analysis requirements. (Goff et. al. 2020'; Wikipedia, 2021)

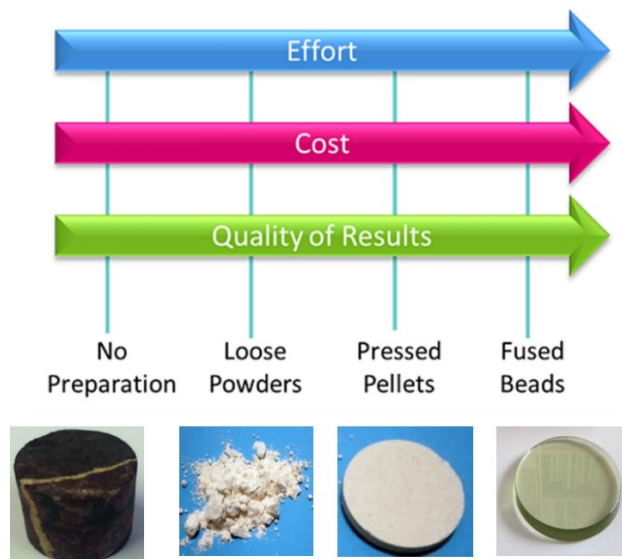


Figure 19. Most common ways to prepare samples for XRF analysis

- *Solid samples* (with no preparation) can be anything from pieces of metal or electronics or plastics to cut and polished metal samples. The ideal sample for XRF analysis will have a perfectly flat surface. Irregular sample surfaces change the distance from the sample to the x-ray source and introduce error. Moreover, if the surface is rough, it can cause scattering and re-absorption of longer wavelength elements.
- The analysis of *loose powdered material* usually requires that the sample be placed into a plastic sample cup with a plastic support film. This insures a flat surface to the X-ray analyzer and the sample to be supported over the X-ray beam. The more finely ground the sample the more likely it is to be homogenous and have limited void spaces providing for a better analysis. Sufficient powder should be used to insure infinite thickness is obtained for all of the elements of interest.
- *Pressing powder* into pellets is a more rigorous sample preparation than pouring loose powders into a sample cup. The process includes grinding a sample into a fine powder, ideally to a grain size of <75um, mixing it with a binding /grinding aid and then pressing the mixture in a die at between 20 and 30T pressure to produce a homogenous sample pellet. This sample preparation approach provides better analytical results than loose powders because the grinding and compression creates a more homogenous representation of the sample with no void spaces and little sample dilution. This leads to higher intensities for most elements than loose powders.
- Sample prepared as *fused beads* provide a near perfectly homogeneous representation of the sample to the XRF and is considered by many to be the ideal sample preparation method for solids. Fused beads are created by mixing a finely powdered (<75um) sample with a flux in a flux/sample ratio of 5:1 to 10:1 and then heated to 900C-1000C in a platinum crucible. The sample is dissolved in the flux (often a lithium tetraborate) and cast into a mold with a flat bottom. The resultant glass disc or fused bead is a homogenous representation of the sample free of mineral structures.

2.2.11. XRF Calibration and Matrix Effect Correction

Quantitative XRF should provide a means of converting the measured XRF spectra to the actual chemical composition of the sample. This is accomplished by modeling a relationship between the intensity of fluorescent X-rays and concentration of samples with known composition. Usually, the higher the concentration of element, the higher will be the count intensity in its corresponding energy channel. Obtaining this calibration function is the main objective of all quantitative XRF analysis methods (Dunlea et. al. 2020; Richard et. al. 1996).

Ideally, converting photon count-rates into elemental concentrations would appear to be straightforward process which might be expected to hold a linear relationship because the rate of generation of x-ray photons is proportional to the element concentration. However, "matrix effects (absorption and enhancement)" complicates the modeling process (as discussed in section 2.2.9) (Dunlea et. al. 2020; Richard et. al. 1996). Therefore, calibration and quantitative analysis of XRF generally consists two-step process; spectrum processing and matrix effect corrections.

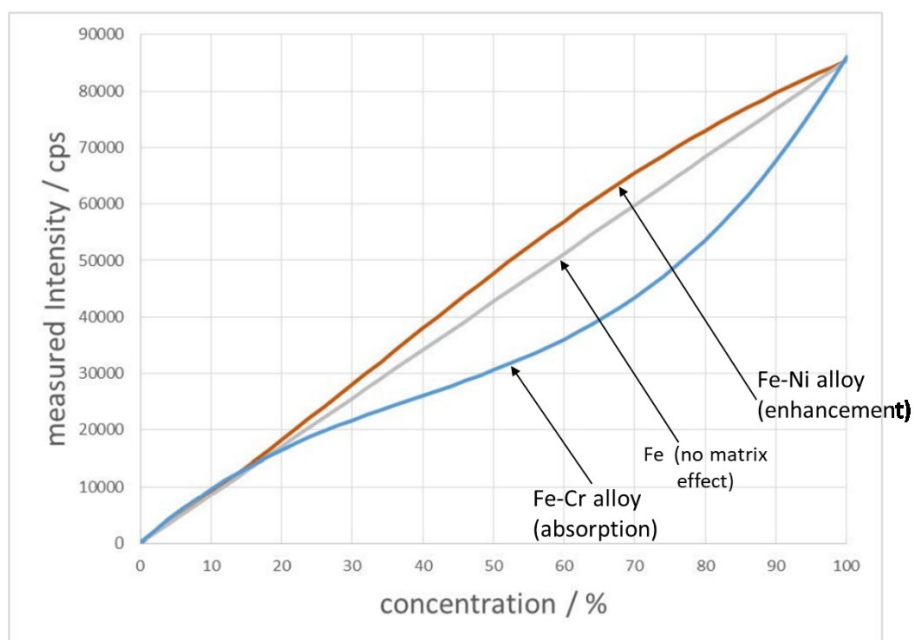


Figure 20. Inter-element matrix effects (absorption and enhancement) (Bruker, 2017).

As shown in Figure 20, for samples which is made up of of only one element, the ideal linear correlation holds. But in reality, where samples such as rocks contain many elements, inter-element matrix effects (absorption or enhancement) cause deviations from perfect linearity. Therefore, quantification models that correlate measured intensities to elemental concentrations should correct the matrix effect (Bruker, 2017; Richard et. al. 1996; Gullayanon, 2011).

Depending on the complexity of samples, these calibration models can be of different complexity (Gullayanon, 2011; Bruker, 2017). Generally, calibration and matrix effect correction procedure can be classified as either:

- *Empirical*: known reference materials are measured and their elements' x-ray line intensities are plotted against their known concentration establishing a relationship (calibration curve) between both. The simpler empirical methods may be constructed without any knowledge of XRF principles (knowledge of instrument and material parameters). Two empirical methods widely used in commercially available XRF instruments are: (Gullayanon, 2011)
 - *The Lucas-Tooth and Price*: uses linear interpolation and. Short coming of such method is the inter-element matrix effect that are caused when the XRF intensity from one element is absorbed by, or enhanced by, another element.
 - *The Lucas-Tooth and Pyne algorithm*: uses a non-linear interpolation step to correct for inter-element interactions.
- *Physical models (Fundamental parameter methods)*: are based on theoretical knowledge of the physics of X-rays and probabilities of physical processes taking place. No standards (or samples with known composition) are needed for this method. These methods utilize only knowledge of instrument and material parameters such as theoretical X-ray beam intensity, beam and detector angles, inter-element effects, and spectral background (Gullayanon, 2011; Bruker, 2017).
- *Mixed models*: are either standard-supported Fundamental parameter method or fundamental parameter-supported empirical method. This calibration procedure is the most used one by XRF analyzers (Bruker, 2017, Dunlea et. al. 2020).

2.3. Drill-Core Scanning

2.3.1. Why Develop Drill-Core Scanning?

Mineral exploration campaigns often collect tens of kilometers of drillcores from subsurface. The recovered drillcore contains the most essential information which is the basis for the resource characterization, reserve estimations, economic and environmental feasibility studies, future mine planning as well as processing flowsheet design. Drilling is expensive operations which often covers the major expense of exploration projects and thus the information carried by the cores should be exploited to its fullest extent (Erickson et. al. 2005).

Conventionally, drillcore logging is carried out by geologists in core-shed where structural, lithological, alteration, core recovery and meta-data (drillhole location, date, core diameter etc.) are all visually examined and recorded. Although conventional core logging has been common practice throughout the mining industry for decades, it is time-consuming and expensive methodology. It also suffers from several limitations. First of all, even though core mapping and logging is a highly specialized skill that requires experience, careful observation, accurate recording, and considerable discipline (Erickson et. al. 2005; Whateley et. al. 1996). Furthermore, any task performed by human operators is always subject to human mistakes. The mapping geologist might misinterpret certain features or overlook features that are too small to accurately determine by the human eye. On top of this the core-logging of a vast amount of drillcore is too big of a task to be performed by a single geologist. It is, therefore, carried out by teams of multiple geologists. Thus, interpretation of cores, no matter how systematic the procedure is followed, will always partly be subjective. Specific geologists might thus have a minor bias in interpreting drillcore features in relation to other geologists (Kruse, 1996; Quigley et. al. 2009).

To accelerate the drill-core logging procedure, reduce interpretation errors and reduce costs automation of core logging is a promising solution. For a long time, a wide range of measurement techniques, such as XRD, XRF, SEM-based analyzers (MLA, QEMSCAN), have been available to aid drill core characterization. Unfortunately, all these techniques share the limitation that they are time-consuming, require extensive sample preparation, might be destructive, analyze only small fraction of the entire collected cores, and have to be performed in specialized labs (Kruse, 1996; Quigley et. al. 2009).

The possible advantage of sensor-based drill core scanning over these techniques is clear. It could provide a fast, non-destructive, and cost-efficient technique for interpretation of big amount of drillcore samples (Quigley et. al. 2009). One of the first studies which investigated the application of hyperspectral imaging for core-mapping was performed by Kruse (1996) using a handheld point

spectrometer. Promising results initiated the production of more advanced and automated systems over the following years.

Although hyperspectral imaging have been a dominant technology for automated drill core logging systems, other sensors are continuously being integrated to the core scanning systems such as X-ray transmission (ANCORELOG), RGB line camera (DMT Corescan³), XRF (Geocore), LIBS (Spectral industries) and Raman (T-REX-ANCORELOG). Unfortunately, the mining industry is traditionally a bit conservative sector and only tends to adopt to new innovations once its benefit has been proven extensively. Therefore, the development of core-scanning systems has been relatively slow, especially considering its potential (Quigley et. al. 2009).

On the other hand, it should be noted that although sensor-based drill-core scanning is a very promising technology, it comes with vast amounts of data (“big data”). The interpretation of this data, which is key to gaining correct mineral information, requires an outstanding know-how of the mineralogy and rocks involved. Several software systems and algorithms have been developed to perform interpretations. But many of these are not yet designed to handle complicated mineral mixtures and can, under the wrong circumstances, easily produce inaccurate logs. Thus, there is always a big room for further researches and innovations of automated core logging. (Rivard et al. 2011).

2.3.2. Commercial Drill Core Scanners

In addition to the systems which are under R&D such as the ANCORELOG, several core-scanning systems are already released on to the market. Below is a short summary of some of the notable systems:

1. *DMT CoreScan³*: The CoreScan3 (shown in Figure 21) is developed by the Germany-based producer DMT and has been active on the market since 20 years. It is different from other scanners in such it only applies measurements in the visible range (RGB line camera). Cores are placed on two rotating cylinders so that a 360° image can be taken. In this setting the system is able to log 3 meters of core per minute. The system comes with an internally developed software, with several features ranging from the calculation of color distributions to geotechnical parameters measurement such as RQD. Besides the software analysis capabilities, a major benefit of this system is that the digital drill core data is stored in an archive becomes much more easily accessible compared to physical drillcores (DMT Group, 2021). Since the CoreScan³ only utilizes photography in the visible range, its applications for mineralogical mapping and interpretations are very limited.



Figure 21. DMT manufactured CoreScan³ (DMT Group, 2021)

2. *MINALYZER CS*: was developed and commercialized by Sweden-based Company, Minalyze AB. This innovative drill core scanner semi-automatically analyses drill cores directly in core trays with X-ray fluorescence spectrometry. Moreover, it is equipped with high-resolution RGB line scan camera that produces digital photo documentation of the drill cores and trays. The XRF sensor is based on energy-dispersive spectrometry (EDS), using a silicon drift detector (SDD). The advantage of this system is that several X-ray tubes with different anode target materials are available (Cr, Mo, and Ag). The selection of anode material depends on the project-specific analytical preferences. (Sjöqvist et. al. 2015)



Figure 22. MINALYZER CS (Sjöqvist et. al. 2015)

3. *OreXplore Geocore X10*: The Geocore system performs XRF measurements. It is being developed by a relatively young, Sweden-based company under the name of OreXplore. Utilizing a system called AXM (Attenuation and X-ray Fluorescence combined measurements), it claims to be able not only to measure elemental concentrations down to 1 ppm, but also able to characterize mineralogy, texture, geological structures and density in three dimensions using the XRF sensor. It can only handle core up to NQ diameter and can only measure one piece of core of length up to 1 meter at a time (Figure 23). (Orexplore, 2021; Bergqvist et. al. 2019).



Figure 23. OreXplore Geocore X10 (Orexplore, 2021)

4. *TERRACORE*: TerraCore Geospectral Imaging is USA based company that was founded in 2015. In partnership with SpecIm (Finish company), one of the world's leading manufacturer of hyperspectral cameras, *TERRACORE* is able to commercialize several core scanning products such as the Sisurock and SisuMobi. The HIS camera is able to combine three different infrared ranges in addition to the RGB images. Comparing the technical specifications of the *TERRACORE* Sisurock with the other hyperspectral systems, the major differences are in the spectral and spatial resolution. The spectral resolution of the Sisurock is below that of the other systems while its spatial resolution is superior (Yousefi et. al. 2020).



Figure 24. TERRACORE SisuMobi (TerraCore Geospectral Imaging, 2021)

5. *Corescan HCL*: The Australian company Corescan produces a hyperspectral core-scanner under the name of HCL (Hyperspectral Core Logger). The Hyperspectral Core Logger (HCL) integrates VNIR-SWIR-MWIR-LWIR spectroscopy, core photography and 3D laser profiling to deliver full range hyperspectral scanning system. All sensors are housed within a 3-axis translation table that allows core trays, rock chips and other sample material to be handled automatically (Corescan, 2021; Jackson, L. M., 2020).



Figure 25. Corescan HCL (Corescan, 2021)

6. *SPECTRAL Industries and Avaatech B.V (LIBS + XRF)*: SPECTRAL Industries is an EIT Raw material supported company that is based in Delft, Netherlands. It specializes in producing LIBS based optical sensor systems for chemical analysis applicable to mining, recycling and material processing. The core scanning system is based on Avaatech's XRF core scanner on which the LIBS instrument developed by SPECTRAL Industries was integrated. According to Dalm (2019), the aim of the collaboration between Avaatech and SPECTRAL Industries is to combine the strengths of both XRF and LIBS technologies to develop a more powerful core scanner that can provide fast and reliable chemical data for a wide variety of applications (Dalm et. al. 2019).

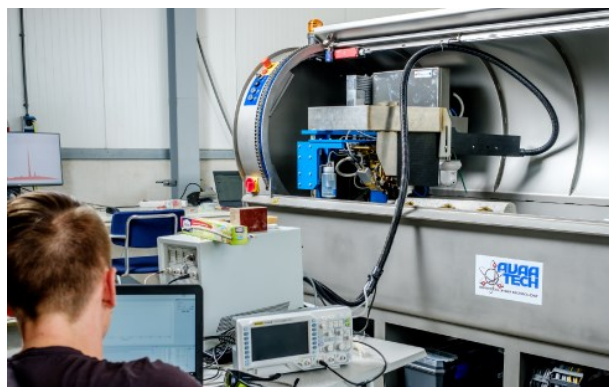


Figure 26. LIBS-XRF core scanner prototype developed by SPECTRAL Industries and Avaatech's XRF core scanner (Dalm et. al. 2019)

3. MATERIALS AND METHODS

3.1. Samples Analyzed

3.1.1. Drillcore Sampling

Logged samples from several drill holes were selected by exploration geologists at Minas de Aguas Teñidas, Spain. MATSA provided a large set of core boxes containing 198 pieces of half-cores originating from the Aguas Teñidas and Magdalena ore deposits. Each piece of core is between 15 and 40 centimeters in length with a diameter of either NQ, HQ or PQ. At earlier stages of ANCORELOG project, the drill cores were used for DSLR photo documentation, generation of lithological database, SWIR hyperspectral image acquisition and P-XRF (portable XRF) analysis at the University of Liege, Belgium.

The samples were selected from 7 different exploration drillholes with each sample individually labelled as belonging to a certain lithology (Table 1). Each sample was accompanied by a brief description from MATSA geologists who did the logging. However, the sampling procedure used by MATSA to select these specific samples is unknown. It remains still unknown if MATSA attempted to select a set representative samples for ANCORELOG that reflects the geological variability of the deposit or not. It is therefore difficult to say if these samples do span the entire range of geological features such as elemental and mineralogical compositions. Additionally, assay values and other lab test results for the selected samples were not provided.

Table 1. MATSA deposit lithological classification

Lithology Class	No.
Breccia	2
Basic	26
Green Tuffite	3
Dacites	17
Red lava	7
Black Rhyolite	14
Rhyodacites	5
Rhyolite	20
Massive Sulfides	15
Stockworks	20
Shale	6
Purple Shale	7
Grey Tuff	26
Rhyolitic Tuff	30
Total	198

The samples include both barren and mineralized units of the deposit. In order to reflect distinct mineralogical and textural patterns, more than one sample was collected from each rock type. For the purpose of further sampling, the most representative extremity of each sample was further sliced to generate small pieces with smooth surfaces 2 to 3 cm wide (Figure 27). The remaining largest portion of the cores are retained in core tray for future uses.



Figure 27. Rock pieces sliced from the main drill-core samples.

3.1.2. Samples description

Most sampled rocks consist of intermediate to felsic volcanic and volcano-clastic assemblages which suggests that these are the most common host rocks in the Magdalena deposit. A few shales and mafic intrusions were also included comprising less than 10% of the total number of samples. Among the 35 mineralized samples, 14 are considered to be massive sulphides and remaining 21 are stockworks.

Lithologies with close composition such as dacites and rhyodacites were combined into the same category by logging geologists. As it occurs in other areas of the IPB, shales are differentiated according to their chemical composition in to black shales and purple shales. Similarly rhyolitic rocks were classified into rhyolites and black rhyolites. Tuffs are mostly separated not only according to their composition but also according to textural variabilities into rhyolitic tuffs, grey tuffs and heterogeneous tuffs. Brief summary of all the lithological classes along with their RGB images is given in Appendix II.

3.2. XRF Instrumentation

3.2.1. XRF Hardware Equipment (J&C Bachmann TEXAS)

The XRF instrument used in this study is called “TEXAS”. It is manufactured by J&C Bachmann GmbH, Germany based manufacturer. This device has been deployed in multiple sites on feed belts, where it can be incorporated into existing processes and the ore can be transported into the path of the incident beam. The XRF measurement system used for this study is basically a “TEXAS” that has been specifically tailored for ANCORELOG.

This instrument consists of X-ray tube as x-ray source, a molybdenum (Mo) anode target, SDD detector and a detachable vacuum chamber. This device is capable of generating a primary X-ray beam source up to 65 KeV in power and up to 15 μ A in intensity. This device is capable of detecting elements from Sulfur to Uranium (U). The penetration depth of TEXAS is approximately 0.1 mm for steels and 1-2 mm for aluminum. Table 2 shows summary of TEXAS XRF device specifications.

Table 2. Device specifications of the TEXAS XRF

Specification	
Detection limit (DL)	10 ppm
Detection range	Sulfur to Uranium
Sensor box dimensions	400*300*220 mm ³
Maximum voltage	65 kV
Power	30W
X-Ray Tube	RTW MCB Mo
Anode target material	Molybdenum (Mo)
Detector type	SDD manufactured by Amptek
Detector area	25mm ²
Spatial resolution	2mm to 5 mm
Exit window	Be (Beryllium)
Collimator	Aluminum slit of size 1mm x 8mm

The TEXAS sensor box (Figure 28) contains all components necessary for an XRF measurement. This device requires two sources of current: a high voltage source (more than 20 kV) generated by an x-ray generator in the control cabinet and provided by the purple HV cable on the right side of the image, and a filament current, which provides current to a tungsten filament within the tube, from which electrons are accelerated toward the metal target. The sensor box also has a cooling system installed to prevent over-heating.

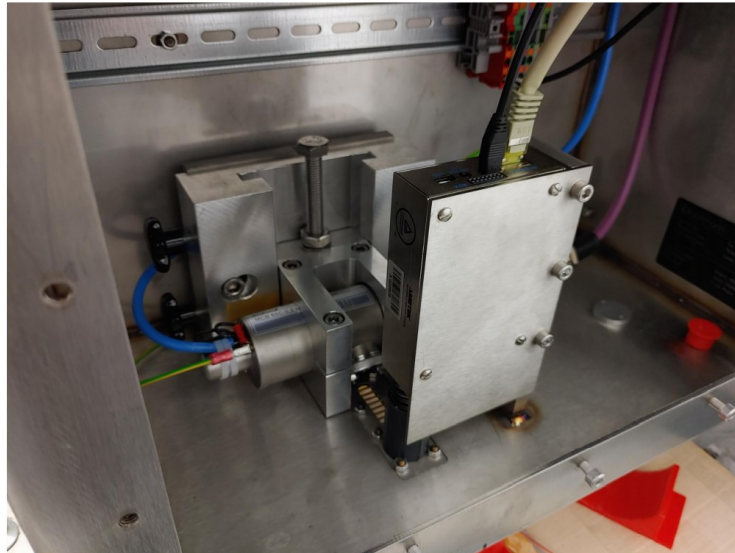


Figure 28. Interior of TEXAS sensor box. This box contains an x-ray tube (rear of box, with yellow warning label), an energy-discriminating detector (front of box) and a cooling system.

3.2.2. Software Suite

The TEXAS Software Suite consists of multiple software modules including hardware control module, XRF numerical analysis, module for on-line process control, module for probe control and module for calibration. Of these, two suites of software that are utilized in this study to acquire XRF spectra from the instrument and process the spectra are briefly described below:

1. *Data Acquisition Software:* XRF spectra can be acquired from TEXAS XRF instruments through J&C Bachman supplied web-based application and, depending on the configuration, the software can be accessed via a WLAN or LAN connection using a laptop, a tablet or even a smartphone. The software is capable of recording XRF count data in a specific data format (*.json files). These specially formatted files contains raw count rates, energy channel for each energy channel and all instrument parameters. The software also displays the XRF spectral plots (Figure 29).
2. *Signal Processing Software:* The TEXAS signal processing software used in this research is based upon SpecQL. It is designed to import XRF measurements in a spreadsheet format, eliminate any unwanted noise in the signals, extract necessary XRF counts, and perform XRF calibrations. This module contains three subcategories; signal processing, database management, and calibration functions (Figure 30).

3.3. ANCORELOG Core-Scanning Prototype

The ANCORELOG prototype (Figure 31) is a three-axis (X-Y-Z) linear motion scanning system which was constructed by DMT to control the position, the speed and data acquisition of several sensors that are assembled to the system resulting in a more accurate and more precise measuring system than could be obtained with hand held measurements..

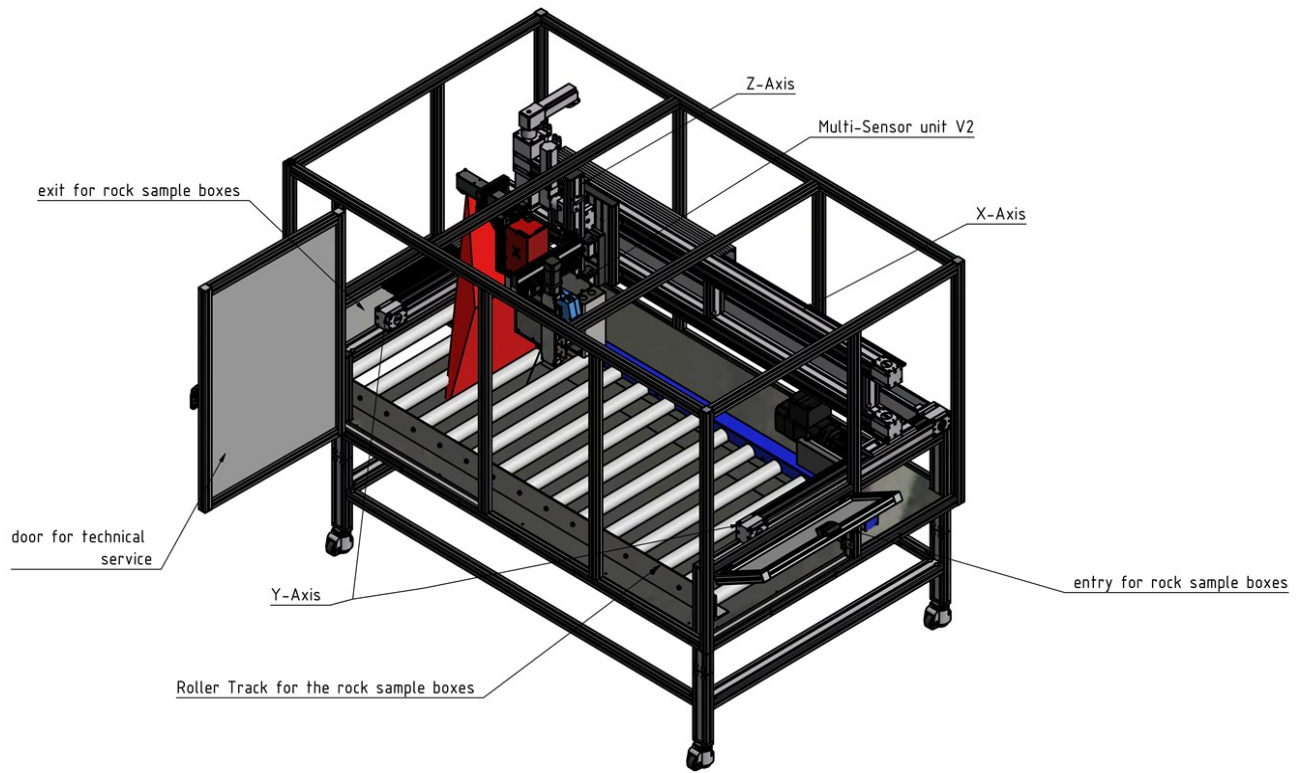


Figure 31. ANCORELOG Prototype (DMT, 2021)

As shown in Figure 32, the “multi-sensor unit” consists of

- Laser line sensor to acquire the height profile of samples in core tray (with 0.1 mm precision).
- Three-axis motion control sensors (with 0.01 mm precision).
- XRF sensor.
- Hyperspectral camera (HSI) in SWIR region.
- Timegated Raman sensor (T-REX).
- And can also mount potential sensors such as RGB camera, LIBS sensor and magnetic sensor in the future.

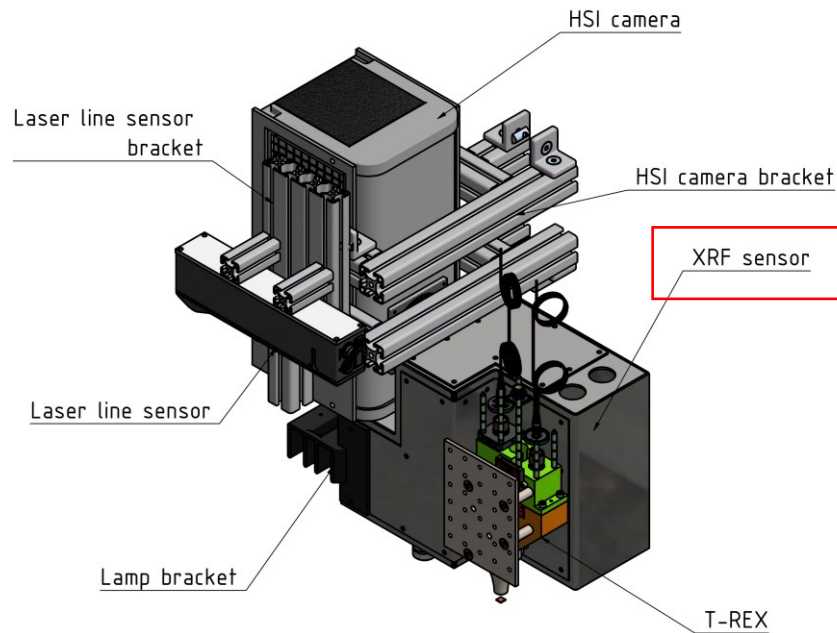


Figure 32. ANCORELOG multi-sensor unit (DMT, 2021)

For this study, the XRF data spectra were acquired using J&C Bachmann XRF sensor assembled to the ANCORELOG scanning prototype. This scanner system is capable of positioning the XRF instrument over an entire core tray. The general scanning settings are illustrated in Table 3. Specification of the XRF sensor is given in section 3.2.1.

Table 3. Operation Settings selected for XRF sensor scanning.

Settings	Value
Scan –speed (mm/s)	1
Spatial resolution (mm)	5
Sample to sensor distance	2 to 5 mm
Current (mA)	0.6
Voltage (kV)	30
Data acquisition mode	continuos

The data acquisition was carried out with the “Continuous measurement method” which is implemented by scanning the XRF instrument across the sample as count data is collected. The moving speed of the XRF instrument must be slow enough to obtain a statistical number of counts at each sample position. In total 3 boxes of drill core samples (198 core units) were collected with scan speed of 1 mm/sec using continuous mode of data acquisition.

The procedure employed can be summarized with the following points:

- Prepare core samples into tray (Figure 33).
- Load the core tray in scanning stage of the ANCORELOG prototype.
- Full-Tray laser height scanning (0.1 mm precision) and thus obtain height profile map of the samples (Figure 34).
- XRF scanning line by line (with scanning speed of 1mm/sec and spatial resolution of 5 mm).
- Spectra generation: three options are available:
 - Integrate over segment/distance: a separate average spectrum generated for each core sample. This research employed this setting as the core samples are small (2-3 cm height).
 - Integrate over time: a spectrum generated over a selected time range.
 - Moving interval: based on the principle of moving window.
- Spectra Pre-processing: it is discussed in the next chapter.



Figure 33. Rock pieces sliced from the main drill-core samples (prepared for XRF scanning)

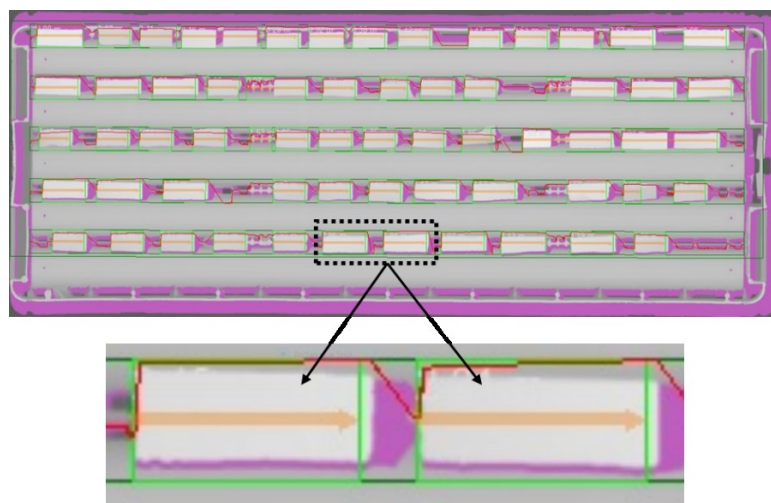


Figure 34. Laser height profile map

3.4. SEM Image Acquisition (ZEISS Mineralogic)

In order to create a direct link between the XRF analysis and chemistry of the drill core units (uncrushed samples), EDX measurements were taken using the scanning electron microscope at the GeMMe SEM lab of University of Liège (Figure 35).

The objectives of the EDX measurements are:

- To relate the XRF spectra of the samples to the elemental distributions provided by EDX scan. In addition to the XRF calibration procedure by chemical analysis (ICP-MS) and pressed pellets, this might give the opportunity to investigate the possibility of calibrating the XRF sensor with EDX alone without depending much on the chemical analysis and pressed pellets.
- When the XRF sensor is calibrated successfully by chemical analysis (ICP-MS) and corresponding pressed pellets, a validation/verification step will be required to test the quantitative calibration models. Drill core units scanned by the SEM-EDS (and thus have known composition) are an ideal samples for this validation process.



Figure 35. ZEISS Mineralogic Scanning Electron Microscope

For a first preliminary study, 16 samples (one per each lithology and 2 for massive sulfide and stockworks) from the dataset were selected. These samples were selected to represent the range of compositions (felsic, intermediate and mafic) within different lithologies of the dataset. The samples used are the small pieces that were cut with a diamond saw into smaller slabs of approximately 2.5-4 cm.

Prior to scanning the samples, optimal settings for the SEM were determined by trial and error. Constraints for the settings were that the scanned area should be 5mm width along the whole length of the core pieces in order to match the spatial resolution of the TEXAS XRF. The final settings used for acquiring EDS images are shown in Table 4.

Table 4. ZEISS Operating parameters

MAP INFORMATION		
Mapping parameter		
Width:	10240	pixel
	54528	μm
Height:	768	pixel
	4090	μm
Pixel size:	5.3	μm
Acquisition parameter		
Pixel time:	32	μs
Overall time:	251	s
Microscope parameter		
High voltage:	20	kV
Working distance:	9	mm
Magnification:	368	x
Sample information		
Name:		
Description:		

4. DATA ANALYSIS AND XRF SPECTRA PROCESSING

4.1. XRF Spectra Qualitative/Energy Calibration

TEXAS ED-XRF detector provides XRF spectra as a plot of intensities (counts of x-rays photons per unit time) versus energy channels. Overall 198 raw XRF spectra were collected, each representing one of the 198 samples. Then the analysis required very precise energy calibration since the measured peaks must be correctly assigned to the individual elements detected in the samples.

The multichannel analyzer of the TEXAS X-ray measurement system measures each signal and then classifies it into one of the available channels depending on the energy (KeV) of the detected photon (see Figure 36). Thus, each channel corresponds to a certain energy range. This means that in order to identify the elements present in each spectra, the relationship between channels and energy must be calibrated.

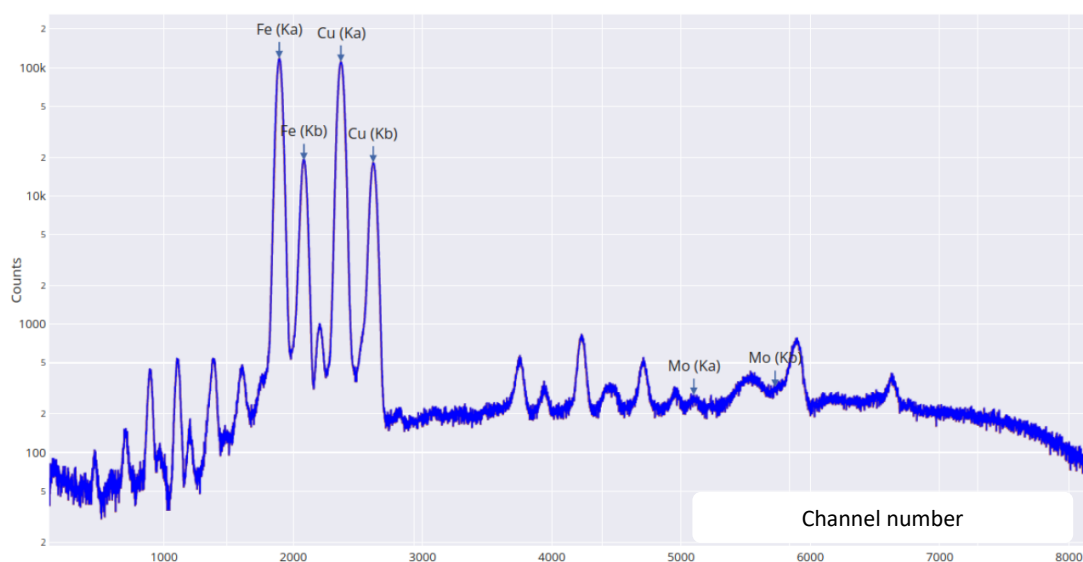


Figure 36. XRF spectra that requires Energy calibration

The energy calibration was carried out using a sample with a known composition (certified reference material). When the raw spectra of the CRM, was generated (Figure 36), the characteristic peaks were selected as reference peaks. For each peak, a corresponding fluorescent peak energy was taken from periodic table of elements and x-ray energies (Appendix III); for e.g. Fe-K α , 6.399 KeV and so on.

Table 5. Selected peaks and their corresponding channel No. and KeV

Element Peak	Channel No.	Energy (KeV)
Fe-K α	2103	6.399
K-K α	988	3.312
Fe-K β	2324	7.058
Ca-K α	1225	3.69

The energy calibration procedure is basically a process of fitting a linear-regression model that inputs channel number (x) to predict photon energy values (y). Theoretically, only two peaks are needed selected because two points are always on a straight line. However, for better calibration's quality, four peaks were used to fit the model. The calibration model has been performed with coefficient of determination (R^2) above 99% (Figure 37). Now, for every spectra generated by the TEXAS analyzer, peaks are easy to be assigned to elements present in the sample according to periodic table of elements and x-ray energies (Appendix III).

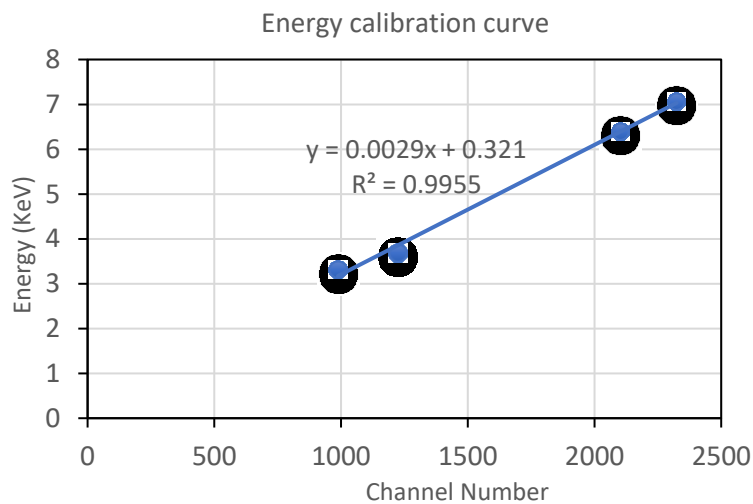


Figure 37. Energy calibration curve

4.2. XRF Spectra Processing

The output of XRF spectroscopy is a plot of counts per second versus photon energies. Figure 38 shows one of the 198 spectra acquired by the TEXAS XRF analyzer. In order to attain the objectives of the project (i.e. identification and quantification of elements in the drill core samples), spectra analysis and processing is required. The procedure employed algorithms that are able to convert the noisy raw spectral counts (orange) all the way to deduce the smooth peak values (pink) and elemental identification (dark holes).



Figure 38. Raw and processed spectrum

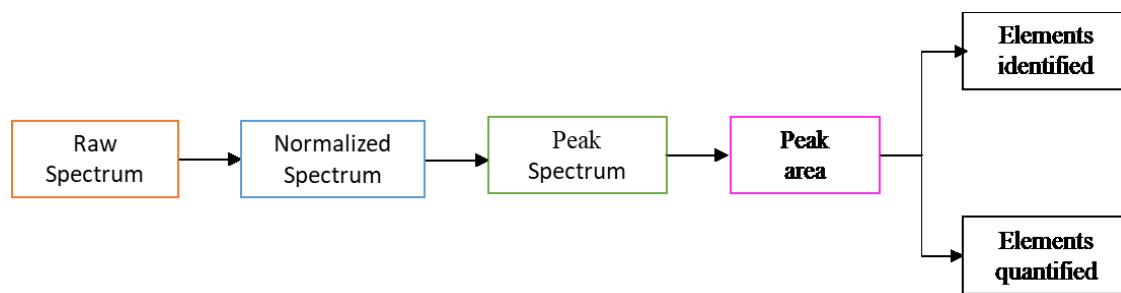


Figure 39. XRF spectra processing and analysis

As illustrated in Figure 39, the major steps of the XRF analysis can be summarized as:

- *Raw Spectrum (orange)*: represents raw values of the spectrum. These noisy points are the original and unprocessed measurement values of the detector system. As it can be seen from Figure 38, the raw count rate went through a step of *temporal spectrum normalization* (to 120s). The temporally normalized raw data is less noisy and enables us to clearly identify low intensity peaks.
- *Normalized (average) Spectrum (blue)*: was determined by averaging the raw count points of adjacent channels in order to reduce statistical fluctuation. After this procedure, the peaks are somehow easy to search and quantify them.
- *Peak Spectrum (green)*: The peak spectrum is determined by subtracting *background/continuum* (red) from the *normalized spectrum* (blue). Background spectrum estimation and filtering (substation) algorithms were employed for this purpose. The Peak-stripping method

was used to estimate the background and then it was subtracted from the average spectra to determine the peak spectrum. Details of Peak-stripping method is in Appendix IV.

- *Peaks and Peak Areas (pink)*: Elemental peaks were then detected and the under each peaks was estimated by fitting Gaussian curves via the Levenberg–Marquardt algorithm. Details of Gaussian fitting are given in Appendix V. The areas under these Gaussian curves represent the final measured values (intensity) and is exported as .CSV file. Appendix VI.
- *Elements (holes)*: The lines of the elements used for the calculation of the peak areas are indexed on the horizontal axis according to their tabulated characteristic X-ray fluorescence photon energies. Elements could be easily identified and marked by looking at the mid-point under each peak and referring to periodic table of elements and x-ray energies (Appendix III). For overlapped or very close peaks, attempt was made for alternative peaks (e.g. Arsenic As-K α emission is at 10.54 keV, and Lead Pb-L α emission is almost identical at 10.55 keV. In this case Arsenic As-K β was used to avoid error).

Once elements are identified (qualitative analysis), the next objective was to quantify the concentration of the elements in the sample (ppm or weight %). This requires quantitative calibration of the XRF sensor by measuring samples of known composition and is discussed in section 5.2. For such calibration efforts, the area under the Gaussian peaks are used as feature for training the calibration models.

5. RESULTS AND DISCUSSION

5.1. Supervised Classification of Lithologies Based on XRF Spectra

Fast classification or clustering of rock samples based on mineralogical or chemical composition can be efficiently performed through supervised and unsupervised Machine Learning (ML) methods. The objective of supervised classification in this case is to assign the drill core segments to a known lithology based on their XRF spectra peak intensity. The machine learning classification produces trained models in which the lithology type and spectrum are statistically evaluated and similarities with spectra of known origin are identified. Of course, such a procedure is generally not error-free, because the more similar spectra of 2 classes are to each other, the more difficult the distinction becomes. Once the models were trained, they were tested on new dataset (validation).

In order to achieve a good classification accuracy, the system needs a sufficiently large dataset of spectra to train the classifier so that the algorithm can recognize the characteristic differences of the drill core spectra.

5.1.1. Defining Datasets, Classes and Features

During the XRF data acquisition, 198 spectra were collected and processed. They represent 14 lithologies as shown in Table 6. However, because of their similar composition, some lithologies have very similar XRF spectral (peak intensities). This makes the supervised learning very difficult and confuses the models. For e.g. Rhyolite and Rhyolitic Tuff are initially assigned into two separate classes (label-1) because of the variation in texture of the rocks. But both are felsic (acidic rocks) with similar composition. Therefore, attempt is made to merge similar lithologies into common class (label 2). With such labeling, the training dataset comprises 198 data points of 5 classes.

Table 6. Dataset for supervised classification

Label 1	No	Label 2	No
Massive sulfide	15	Massive sulfide	15
Stockworks	20	Stockworks	20
Black Rhyolite	14	Felsic	62
Rhyolite	20		
Rhyolitic Tuff	28		
Breccia	2	Intermediate	57
Green Tuff	3		
Dacites	17		
Rhyodacites	5		
Shale	5		
Grey Tuff	25		
Basic	25	Mafic	38
Red Lava	6		
Purple Shale	7		
		Dataset	198

Before attempting any classification of the samples, it is required to understand what are the features that better characterize the data set and their statistical distribution. Table 7 shows all possible features extracted from the spectra.

As expected, Fe ($K\alpha$) peaks is a spectral feature that shows a good “discrimination power” between the 5 types (classes) of rocks (see the scatter plot in Figure 40). For the lower ranked elemental peaks (such as As- $K\beta$), a large range of overlap is observed between the classes, thus it can be expected that this feature is not the most relevant for classification purposes. During training, first, all of the features were used in the classification. Then, different approach was implemented by identifying and selecting only those features (peaks) that allow the sharpest distinction between the different rock classes.

Table 7. Features' ranking based on Gain Ratio.

Feature	Ranking
Fe (K α)	1
Cu (K α) + Zn (K α) + Pb (L α)	2
Cu (K α)	3
Zn (K α)	4
Pb (L α)	5
S (K α)	6
Mn (K α)	7
Co (K α)	8
Cd (K α)	9
Ag (K α)	10
As (K β)	11
Si (K α)	12

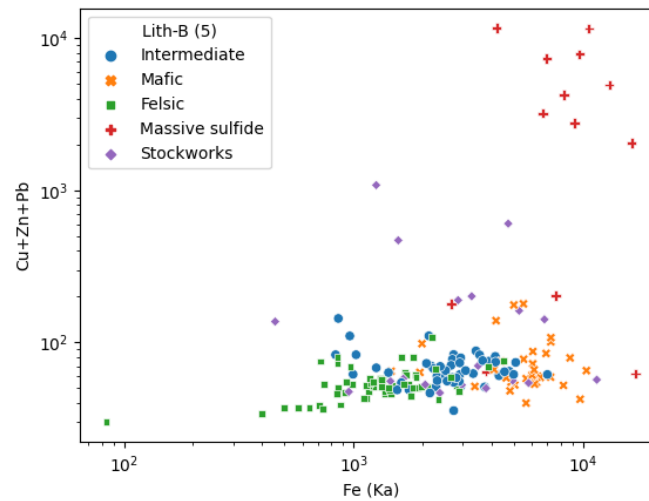


Figure 40. Scatter plot of Fe (K α) versus Cu (K α) + Zn (K α) + Pb (L α)

5.1.2. Training and Testing (Validation)

Four classifiers were applied to the dataset. The classification results is shown in Table 8 for the four different methods. All the methods allow obtaining comparable classification results. XGBoost showed the best separation between the rock classes (72.6 % accuracy).

Table 8. Classifiers accuracy

Classifier	Classification Accuracy
Random Forest	0.712
Logistic Regression	0.690
N \grave{a} ive Bayes	0.709
XGBoost (Decision Tree based)	0.726

5.2. Calibration of TEXAS XRF Sensor for Quantitative Analysis

After the energy calibration step, the peaks visible in the spectra were assigned to an element in the sample based on its photon energy. The number of counts in each peak minus a background value is approximately proportional to the corresponding element's concentration (wt% or ppm) in the sample. Quantitative calibration refers to the process of quantifying the relationship between an element's sample concentration and the number of counts in the corresponding peak. The calibration of the elements to be measured is carried out based on the measurements performed and the corresponding concentrations made by other analytical techniques (ICP, LIBS, portable XRF...).

The main challenge of XRF core scanning relative to conventional geochemical analysis is the task of conversion of spectra output to element concentrations. The main reason for this problem is the matrix effect (absorption and enhancement) of rock samples and the poorly constrained measurement geometry attributable to inhomogeneity of the specimens (e.g. grain-size distribution, roughness of surface).

In conventional quantitative XRF analysis under well-constrained laboratory conditions, empirical calibration (conversion of the net intensity of an element to a weight % or ppm) is provided by the following general equation (Jenkins, 1999; De Vries et. al. 2002):

$$W_{ij} = K_j I_{ij} M_{ij} S_i \dots \dots \dots (1)$$

Where:

- W_{ij} = the concentration (weight % or ppm) of element j in specimen i .
- K_j = represents a device-specific calibration constant for element j (the sensitivity or detection efficiency).
- I_{ij} = represents the net intensity (counts per second) of element j in specimen i , obtained by preprocessing of the raw spectrum by background subtraction.
- M_{ij} = is the matrix effect which corrects for scattering, absorption and enhancement effects on I_{ij} caused by the presence of other elements in the specimen.
- S_i = is the specimen effect which captures the measurement geometry and specimen homogeneity relative to the standard configuration.

Under well controlled laboratory conditions, K_j and S_i are constant, and W_{ij} is estimated directly from I_{ij} , with a correction factor given by M_{ij} . The matrix effect is commonly expressed as a function of the concentrations of the other elements present in the specimen that can cause absorption or enhancement of the count rate of the element concerned. Various methods for estimating M_{ij} have been proposed, most of which are based on a combination of theory and empirical methods

(calibration standards). Under ideal conditions, entirely theoretical methods for estimating M_{ij} (so-called fundamental parameter methods) may be utilized to predict net intensities based on known specimen compositions. But the robust methods employ combination of both empirical (sample based mathematical models) and fundamental parameter. Detail on calibration methods is already discussed in sections 2.2.9 and 2.2.11. “Matrix effect parameter M_{ij} is ignored for this study because whole rock chemical analysis of samples that were sent to laboratory could not be delivered by the time the thesis is submitted.”

The common practice to calibrate element intensities (count rates) measured by core scanning XRF is to rely on concentrations obtained by conventional chemical analysis (e.g. ICP-MS) and make use of ordinary least-squares linear regression. After fitting the model, squared correlation coefficients (R^2) is calculated to evaluate if the variation in one in elemental concentration can be well explained by the count rate. R^2 above 0.8 is considered strong correlation.

To achieve the calibration, representative samples that are anticipated to represent all lithologies and cover the entire range of elemental range (especially the valuable metals) and were sent to accredited laboratory for chemical analysis. As shown in the flowsheet (Figure 41), for every rock sample, it will be pulverized first before whole rock analysis by ICP-MS method would be extracted and a corresponding pressed pellet would be made out of the same crushed sample (note: pressed pellets is a robust sample preparation method for XRF measurement (See section 2.2.10).

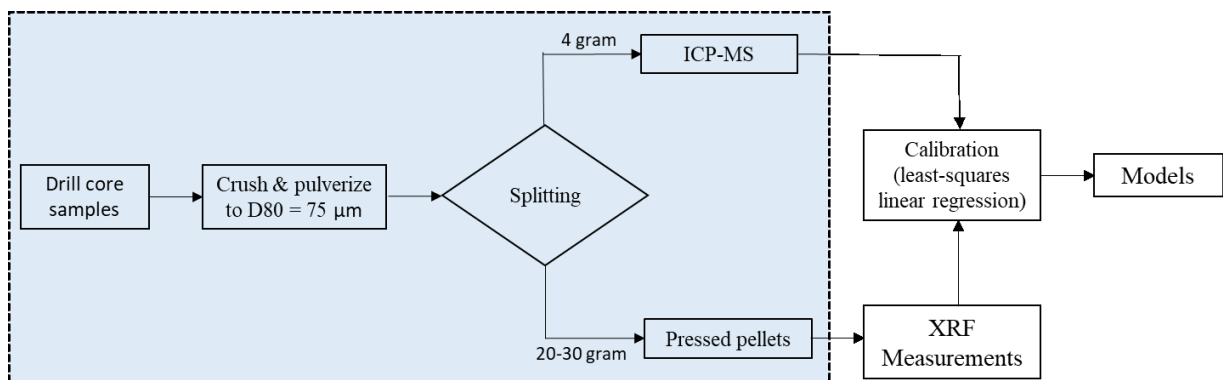


Figure 41. Calibration procedure diagram

However, the laboratory couldn't deliver the results by the time this thesis is submitted. As alternative, an attempt was made to use instead portable-XRF measurements made on the drill core to at least come up with “semi-quantitative” calibration models. As it can be seen from Figure 42, models for the 4 main elements of interest are presented (note: the curves for Cu, Zn and Pb are not straight because the linear-regression are plotted on log-scale). All four models show high values of R^2 for linear regression of intensities into weight proportions of corresponding elements. This implies that there is sufficient predictive power of the models within the range of concentrations plotted.

These models can be imported into the TEXAS software suite and therefore future XRF measurements of samples will directly provide weight proportion (wt %) of the four elements present in the samples.

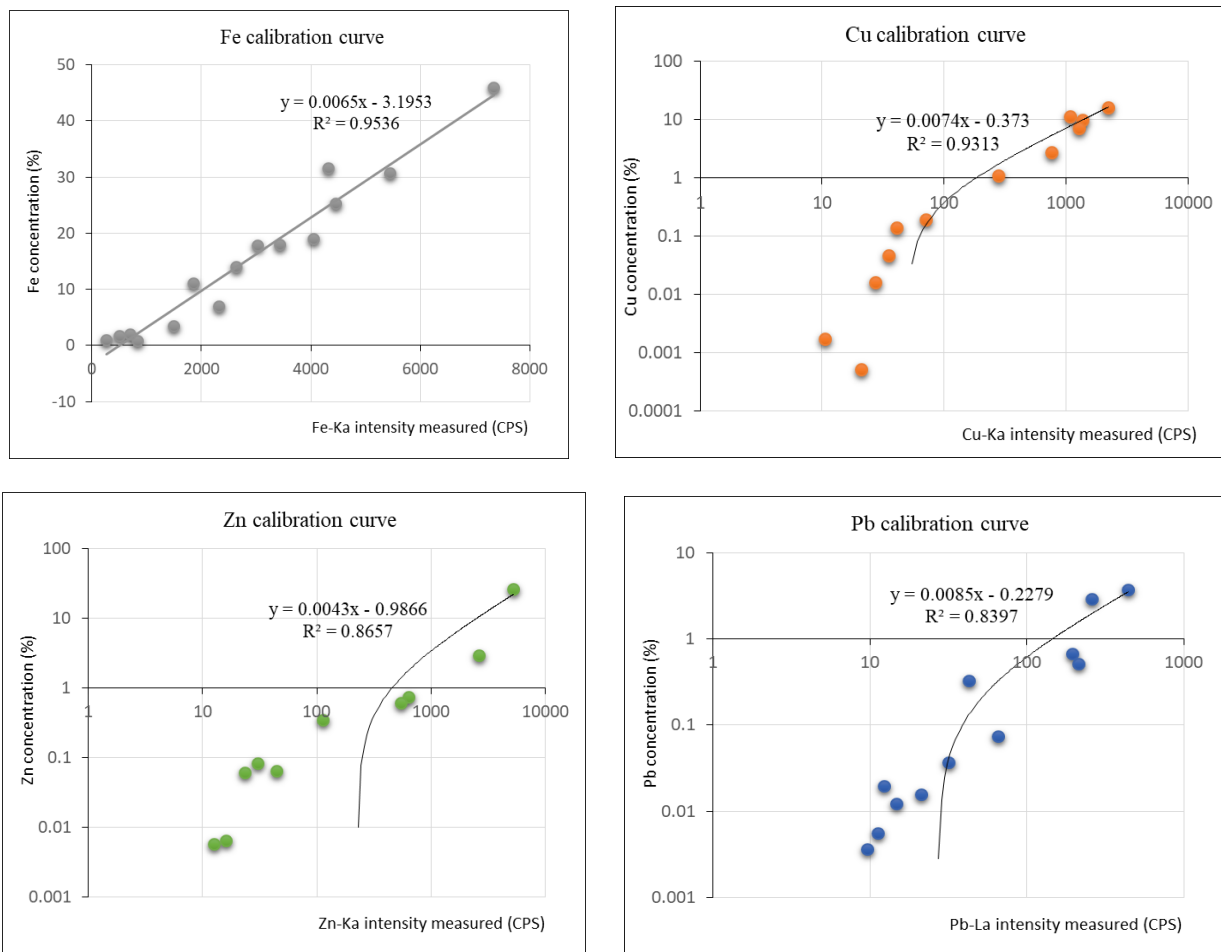


Figure 42. Copper, zinc, lead and iron calibration curves (measured peak intensity values versus portable XRF weight %). Note: the curves for Cu, Zn and Pb are not straight because the linear-regression are plotted on log-scale.

More robust models will be developed once the analytical lab results and pressed pellets are received from the laboratory. Moreover, matrix effect will be estimated and corrected for every elements of interest using combined methods (empirical + fundamental parameter) based upon the whole rock composition.

When the XRF sensor is calibrated successfully by chemical analysis (ICP-MS) and corresponding pressed pellets, a validation/verification step will be performed on uncrushed rock units by the aid SEM-EDS (ZEISS Mineralogic).

6. CONCLUSION AND RECOMMENDATIONS

Traditional drill core logging carried out by geologists is often subjective and time consuming. On this basis, new sensor-based technologies have arisen to solve exploration constraints. ANCORELOG (analytical core logging system) is EIT Raw Materials supported project that aims to automatize core logging with the application of several sensors. This thesis particularly focuses on the integration and calibration of XRF sensor to the ANCORELOG prototype.

Five main objectives have been undertaken in this thesis:

- i. Visual characterization of 198 MATSA core samples drilled from Iberian Pyrite Belt (IPB); followed by classification of the samples into 14 lithologies (12 barren and 2 mineralized lithologies).
- ii. Set up and operation of XRF sensor manufactured by J&C Bachmann into the Analytical Core Logger (ANCORELOG) prototype which has already integrated SWIR camera successfully.
- iii. Processing and analysis of raw and noisy XRF spectra into well-defined Gaussian-fitted elemental peaks and hence identification and quantification of elemental composition of drill core samples (i.e. qualitative and quantitative analysis).
- iv. Developing Linear-regression calibration models to convert the XRF output (count rate) to element concentrations based on known composition samples.
- v. Supervised classification of samples using XRF spectral features into basic lithological classes.

After XRF data acquisition, XRF signals and elemental peaks were obtained by the combined use of signal processing algorithms and operator's interpretation (manual handling of the spectra) of the raw spectra. The analysis applied to the raw spectra (counts versus channels) first involved energy calibration (channel no to energy conversion) followed by manual removal of artifacts; Compton peaks, Rayleigh peaks, sum peaks, escape peaks, deconvolution of overlapped peaks. Then XRF spectrum analysis algorithms were applied for background estimation and Gaussian peak fitting. The resulting spectra showed clearly detected peaks that were assigned to their respective elements.

Therefore, study showed that the ANCORELOG mounted XRF sensor (J&C Bachmann TEXAS) was successful in identifying all elements of interest except silicon (as the SDD detector is made up of silicon material) and thus it could automate the process of geological drill core logging.

Furthermore, this study carried out quantitative XRF analysis to provide a means of modeling the relationship between the measured fluorescent X-ray intensity and the actual chemical composition of the sample. However, the chemical analysis result couldn't be delivered on time due to technical

reasons and portable XRF was used as quick alternative for semi-quantitative calibration. The linear-regression calibration models have shown high values of R^2 (above 0.80) implying that they have sufficient predictive power.

The XRF spectra generated from the ANCORELOG was not only effective in identifying and semi-quantitatively determine sample compositions but was also able to discriminate between rock types (both mineralized and barren) with somehow satisfying accuracy with the aid of machine learning (supervised) algorithms.

In conclusion, it is already stated that the main objective of this work is to evaluate the potential of XRF sensor for automated drill core logging of IPB rocks. The results has shown that XRF integration in ANCORELOG has big potential to significantly enhance the existing capability of the automated core logging system by providing real-time and accurate non-destructive chemical analysis.

As this study is also a basis for future work on XRF drill-core scanning, the following points can be made:

- Obtaining robust calibration function is the main objective of all quantitative XRF analysis methods. Therefore, robust quantitative calibration models and matrix effect correction algorithms will be required to develop based on accurate chemical analysis and pressed pellets.
- Automating the removal of artifacts (Compton peaks, Rayleigh peaks...) from the XRF spectra.
- Evaluating the potential of extending the technique to other deposit types (e.g. magmatic or sedimentary-hosted deposits).
- Integration and implementation of additional sensors to ANCORELOG such as the RAMAN, LIBS and RGB line camera.
- Multi-sensor data fusion based on robust machine learning algorithms such as artificial neural networks.

7. EIT RAW MATERIALS CHAPTER

This study is part of EIT Raw Materials sponsored R&D project under the name of ANCORELOG. It was originally proposed in 2017 with an initial project duration from 2018 to 2020. Although, it got one year delay due to technical reasons, its completion (and demonstration) is expected by end of 2021. The project aims to develop a mobile drillcore logging system that measures chemical, geological, metallurgical and structural rock properties in real-time and hence create a smart classification of the core into domains (classes) based on such properties. This requires innovative handling of ‘big data’ and the integration of multiple sensors into one logging system.

ANCORELOG is conducted by a consortium of several partners. Leading partner of the project is DMT GmbH & Co KG, a company that has been active in the core scanning technology for more than 25 years. The research group GeMMe at the University of Liège is a core partner of the EIT Raw Material projects including the ANCORELOG. It has historically focused on traditional disciplines of ore geology, metallurgy and civil engineering. However, within the last ten years, GeMMe has developed expertise in the area of Geo-Imaging and sensor-based solutions for identification, characterization and quantitative evaluation of mineral resources. Other ANCORELOG partners are listed in Appendix I.

Considered as a twin project and successor to ANCORELOG, Timegated Raman for Exploration (T-REX) was proposed in 2019 by the same consortium under the leadership of VTT (Technical Research Centre of Finland) to EIT Raw Materials. T-REX objective is the development of a novel timegated RAMAN sensor adapted to the requirements of the raw materials sector. The T-REX sensor aims at supplying precise real-time mineralogical analysis of rock samples. The sensor is being integrated into ANCORELOG multi-sensor drill core logging system.

7.1. Impact, Economic Benefits and Sustainability

ANCORELOG will contribute to economic, environmental and social sustainability through more robust exploration, mining, processing and recycling planning. With ANCORELOG technology, industrial companies will make significant savings through an improved energy and material efficiency. The automated and real time analysis of drill cores and cutting samples will help optimize the drilling decisions by enhancing the amount of information that is extracted from the drillcore. Decreasing the quantity of drilling directly and avoiding unnecessary drilling activities resulting in environmental and financial benefits. Furthermore, the continuous chemical and mineralogical analysis of drill core and cuttings and the definition of geological domains will help to reduce the number of samples to be further analyzed and hence impact the social and environmental aspects positively.

An increase in efficiency at the feeding of the material value chain (exploration) generates benefits that will resonate throughout the entire downstream value chain. By the early precise and accurate characterization of geometallurgical domains, planning of mining and consequent processing can be done at a much higher efficiency, potentially increasing overall recovery and decreasing both beneficiation cost and chemical reagents consumption. The final outcome of this could lead to improvements for environments and local communities by a decreased volume of tailings disposed. Universities, being one of ANCORELOG's target customers, will get an academic benefits when purchasing an instrument in order to facilitate the technology to students and research projects. Several students will be involved and get an opportunity to make a master and PhD thesis around this project. Existing contacts to universities outside Europe can also attract students from mining districts outside the EU. Moreover, ANCORELOG will encourage people to create start-ups and small scale businesses that can offer services with ANCORELOG to the RM sector, strengthening industrial competitiveness and increasing employment.

7.2. Business Opportunities

A mining feasibility study is an evaluation of a proposed mining project to determine whether the mineral resource can be mined economically. It is a critical phase of any mining project. Feasibility decisions in the mining sector depend on accurate and efficient processes of drilling results in prospecting, extraction, mining and ore processing operations. ANCORELOG supports these decision makings through a mobile full volume rock analysis system for chemical, physical and structural properties with output available real-time on-site.

ANCORELOG consortium have identified 2 primary target markets and another 2 secondary markets:

- Primary targets:
 - *Mining and exploration companies*
 - *Service and drilling companies and laboratories*
- Secondary targets:
 - *Universities and research institutes*
 - *Geological Surveys and drill-core and sample archives*

Exploration stages of a mining project deal with huge amounts of rocks and soil samples of which only a certain part will be relevant for further mineralogical and chemical analysis. During the mine operations the amount of rock sampled is still huge, where also samples from blast holes are chemically analyzed in order to get a daily ore grade control. Such analysis of samples are either done through time consuming on-site handheld XRF instruments or sent to an accredited laboratory,

where the processing time of samples can take up to weeks and months causing delays (time cost). ANCORELOG offers solution to such challenge by analyzing samples and detect regions of interest in real-time and on-site in order to reduce the number of samples and to concentrate on relevant intervals of drill core or cuttings, significantly speeding up decision-making and lowering time and cost during both exploration and operations.

Secondary targets for ANCORELOG are mostly academics and institutions. The interest for these customers in an analytical core logging instrument would be to provide state-of-the-art technology for research projects.

7.3. Timegated Raman for Exploration (T-REX) and Other Future Works

ANCORELOG have so far integrated Hyperspectral SWIR Camera and X-Ray Fluorescence technologies for supervised classification of core segments into geological domains using machine learning algorithms. However, the integration of a new sensors and smart machine learning algorithms to the study can improve the capability of the automated logging. Some of the principal on-going and future works are described below:

1. *T-REX*: As mentioned earlier, the Timegated Raman for Exploration (T-REX) comprises the development of a novel Timegated RAMAN sensor as a technology used in the raw materials sector for the first time. The project aims at supplying precise real-time mineralogical analysis of rock samples. Mineralogical composition data gathered from the T-REX sensor will flow into ANCORELOG's multi-sensor data fusion approach and enhance ANCORELOG's smart algorithms designed to classify rock samples into geological and geometallurgical domains. T-REX allows a mineralogical sample analysis for on a wide range of minerals including those related to CRM (critical raw materials) such as Lithium (note; lithium is too light to be detected by XRF). Lithium-bearing drillcore samples from Keliber's Lithium Project (Finland) are already in DMT headquarters (Essen, Germany) to be analyzed with the T-REX sensor.

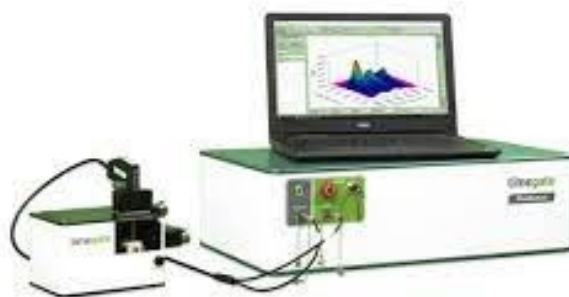


Figure 43. Timegated Raman for Exploration (T-REX) (VTT, 2020)

2. *Laser-Induced Breakdown Spectroscopy (LIBS)*: LIBS is a sensor technique that provides information on a material's chemical (elemental) composition. It utilizes a pulsed laser beam to ablate a small amount of material on the surface of a sample and break it down into a plasma. When the plasma cools down it emits EM radiation and the wavelength and intensity at which these emissions are produced provides information about composition and concentration of the elements present in the sample. The advantage of the technique includes the very low measurement time which makes it reliable for core logging systems. Institute for Geosciences and Natural Resources (BGR), a partner of ANCORELOG, is researching on the potential of LIBS technology for drill core scanning. Moreover, SPECTRAL Industries, from Netherlands has developed LIBS instruments that it claims are powerful tool for analysis for rock samples. Therefore, integrating LIBS sensor into ANCORELOG prototype would open new room for research and improving the system.

3. *Multi-Sensor Data Fusion*: The ultimate objective of ANCORELOG and T-REX projects is fusion of all the data acquired from the multiple sensors. This will be mainly carried out at the University of Liege where the different outputs will be merged in a unique spatial coordinate system. After individual pre-processing is carried out, the SWIR, XRF and Raman spectra will be fused by low-level data fusion. The complete data arrays from each technique will be concatenated into a new, unified matrix and treated as though they were a single spectral fingerprint of a given specimen. A challenge of the data fusion approach consists in defining a way to interpolate punctual values so that the number of measurements can be decreased saving time in operational applications with reasonable deviations. At advanced stages, all the information about the sample including petrographic properties and grades obtained by sensors can be attached to a QR Code which can be used as a fast and informative tool when samples are examined.

APPENDICES

Appendix I. ANCORELOG Consortium.

Appendix II. Brief Description of Lithologies in the Dataset.

Appendix III. Periodic Table of Elements and X-Ray Energies (Bruker)

Appendix IV. Peak-Stripping Method of Background Estimation




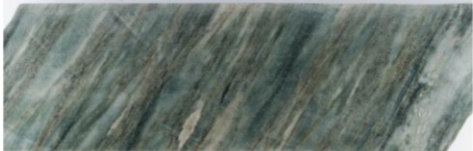


Appendix V. Gaussian Fitting







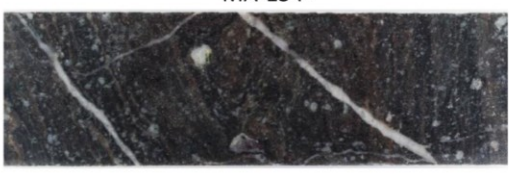

Appendix VI. XRF Spectra Dataset







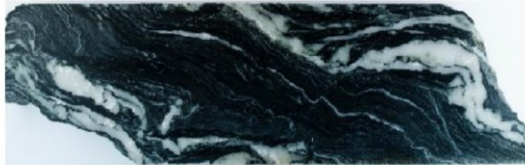

Appendix I. ANCORELOG Consortium.





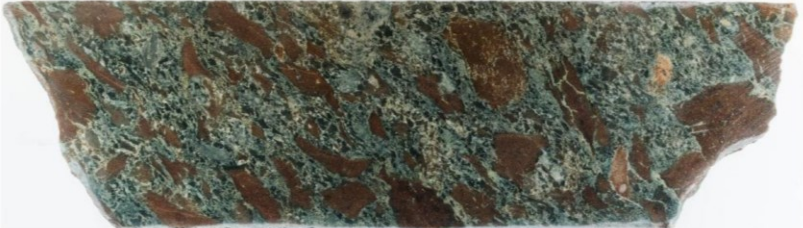
- DMT GmbH & Co. KG, Germany (Lead Partner)
- Université de Liège, Belgium
- Minas de Aguas Teñidas SAU, Spain
- Bundesanstalt für Geowissenschaften und Rohstoffe, Germany
- Catura Geoprojects (Geosciences Conseil), France
- ERAMET Research, France
- Fraunhofer-Gesellschaft zur Förderung der angewandten Forschung e.V., Germany
- Geological Survey of Finland (GTK), Finland
- J&C Bachmann GmbH, Germany
- LTB Lasertechnik Berlin GmbH, Germany
- LTU Business AB, Sweden
- Université Paris Sud-Paris Saclay, France
- VTT Technical Research Centre of Finland

Appendix II. Brief Description of Lithologies in the Dataset.

Basics	<p>The basics lithology covers any volcanic rocks of originally basic composition. This includes for example andesites and diabase. Andesite has been included in this lithology despite it actually being of intermediate composition. Samples from this lithology commonly have greenish colours, porphyritic textures and mafic minerals which makes identification relatively straightforward. Due to overprinting such as silicification, the composition the actual composition can sometimes still be moving towards felsic (see sample MA-154-346). In this case it is the porphyritic texture which tells us the original rock was basic.</p>	
	<p>MA-190-481</p> 	<p>MA-154-346</p> 
Dacites-Rhyodacites	<p>Dacites-Rhyodacites is a lithology which cover the transition into more felsic rocks. The variety within this lithology both in textures and composition is large. Common textures are porphyritic with feldspars crystals (see MA-244-C1-834) and strongly banded or deformed samples (see MA-156-469). Additionally, samples containing heavy hematization and chloritization are common within this lithology.</p>	
	<p>MA-244-C1-834</p> 	<p>MA-156-469</p> 
Rhyolites	<p>Rhyolites is a lithology that covers felsic rocks, which can be identified by their very high feldspar content. See samples MA-190-247 and MA-156-129. Nonetheless, due to alteration phases samples can still have wide varieties of textures and compositions, sometimes shrouding the original composition strongly. Textures encountered within this lithology are e.g. perlitic, peperitic, brecciated and vascular.</p>	
	<p>MA-190-247</p> 	<p>MA-156-129</p> 

Rhyolitic tuffs	Rhyolitic tuffs are one of the volcanoclastic lithologies from Magdalena. Classification of tuffs is often challenging due to their complex nature. Criteria for rhyolitic tuffs are mostly confined to rhyolitic and bright compositions. Textures vary wildly from coarse, to fine grained and undeformed to highly deformed.	
	MA-154-145 	MA-190-84 
Heterogeneous tuffs	One other volcanoclastic lithology within this dataset are the grey and heterogeneous tuffs. For simplicity these are designated as heterogeneous tuffs further on. As the name implies, this lithology comprises of complex tuffs covering almost any composition. The samples are often dark, and frequently deformed with varying clast sizes, veins and veinlets, flow textures etc.	
	MA-45-75 	MA-244-C1-660 
Red lavas	Red lavas are volcanic rocks of basaltic composition with mostly bright red colours. Textures vary from flow textures with large clasts such as sample MA-190-176 to more massive samples. Large quartz veins combined with chloritic alteration (such as sample MA-154-99) are common within the available samples of this dataset.	
	MA-190-176 	MA-154-99 
Black rhyolites	Black rhyolites were originally formed as mafic intrusions that due to silicification have been overprinted into a more rhyolitic composition. The designation 'rhyolite' is therefore slightly deceiving. The samples are frequently dark with quartz veins and vacuoles. Due to the similar compositions the samples can sometimes be easily confused with the rhyolites lithology.	
	MA-154- 	MA- 

Green tuffites	Green tuffites are volcanoclastic rocks of very fine grain-size. As the name implies they are commonly green of colour.	
	<p>MA-45-85</p> 	<p>MA-45-294</p> 
Shales from SU	Only three samples are available which all originate from the same drillcore section. This lithology occurs intermixed with the black shales lithology. Both lithologies are very similar in that they consist of dark, often mylonitized shales. Like all shale lithologies in this dataset, these shales are heavily intercalated with carbonate and quartz veins related to the layered structure of the rock.	
	<p>MA-244-265</p> 	<p>MA-244-278</p> 
Purple shales	The purple shales lithology consists of strongly hematized shales of purple to red colour. For geologists this is an important lithology since it is the only unit that occurs consistently throughout the local geology and therefore is an important stratigraphic marker.	
	<p>MA-244-355</p> 	<p>MA-244-C1-644</p> 
Black shales	Black shales refer to very dark and sometimes bituminous shales. Large quartz/carbonate veins are numerous throughout these samples due to the layered structure of shales. Additionally, related to the rheology of shales they are often heavily deformed.	
	<p>MA-244-263</p> 	<p>MA-244-291</p> 

Massive sulphides	<p>Massive sulphides are mineralised samples with high concentrations of chalcopyrite, galena, sphalerite and/or pyrite. Textures vary from massive, to flow textures, to slightly disseminated sulphides. Depending on the type of mineralization the samples can be either dark or bright.</p>	
	<p>MA-154-274</p> 	<p>MA-190-608</p> 
Stockwork	<p>Stockworks are mineralized samples that are not as massive as the massive sulphides. Sulphides are often present either disseminated or in veins. As expected, most stockworks are found around VMS mineralisation. Sulphide minerals found are mostly pyrite and chalcopyrite but also sphalerite and galena in minor amounts. Apart from the deposition of sulphides, most samples are heavily affected and highly altered by hydrothermal alteration.</p>	
	<p>MA-154-495</p> 	<p>MA-244-157</p> 
Breccia	<p>Only one sample of breccia is present in the dataset. Nonetheless, it is known that this lithology covers volcanoclastic rocks with distinct angular clasts. The clasts are often pinkish colour.</p>	
	<p>MA-154-133</p> 	

Appendix III. Periodic Table of Elements and X-Ray Energies (Bruker)



Periodic Table of Elements and X-ray Energies

www.bruker.com/hhxf

1 H 1.01 0.0007 Hydrogen	2 He 4.00 0.0002 Helium																				
3 Li 6.94 0.53 Lithium	4 Be 9.01 1.85 Beryllium K α 0.108															5 B 10.81 2.34 Boron K α 0.183	6 C 12.01 2.27 Carbon K α 0.277	7 N 14.01 0.001 Nitrogen K α 0.392	8 O 16.00 0.001 Oxygen K α 0.525	9 F 19.00 0.001 Fluorine K α 0.677	10 Ne 20.18 0.0009 Neon K α 0.849
11 Na 22.99 0.97 Sodium K α 1.040	12 Mg 24.31 1.74 Magnesium K α 1.254															13 Al 26.98 2.70 Aluminium K α 1.486	14 Si 28.09 2.33 Silicon K α 1.740	15 P 30.97 1.82 Phosphorus K α 2.010	16 S 32.07 2.07 Sulfur K α 2.309	17 Cl 35.45 0.003 Chlorine K α 2.622	18 Ar 39.95 0.002 Argon K α 2.958
19 K 39.10 0.86 Potassium K α 3.314	20 Ca 40.08 1.54 Calcium K α 3.692 L α 0.341	21 Sc 44.96 2.99 Scandium K α 4.093 L α 0.395	22 Ti 47.87 4.54 Titanium K α 4.512 L α 0.452	23 V 50.94 6.11 Vanadium K α 4.953 L α 0.510	24 Cr 52.00 7.15 Chromium K α 5.415 L α 0.572	25 Mn 54.94 7.44 Manganese K α 5.900 L α 0.637	26 Fe 55.85 7.87 Iron K α 6.405 L α 0.705	27 Co 58.93 8.86 Cobalt K α 6.931 L α 0.775	28 Ni 58.69 8.91 Nickel K α 7.480 L α 0.849	29 Cu 63.55 8.93 Copper K α 8.046 L α 0.928	30 Zn 65.38 7.13 Zinc K α 8.637 L α 1.012	31 Ga 69.72 5.91 Gallium K α 9.251 L α 1.098	32 Ge 72.64 5.32 Germanium K α 9.886 L α 1.188	33 As 74.92 5.78 Arsenic K α 10.543 L α 1.282	34 Se 78.96 4.81 Selenium K α 11.224 L α 1.379	35 Br 79.90 3.12 Bromine K α 11.924 L α 1.481	36 Kr 83.80 0.004 Krypton K α 12.648 L α 1.585				
37 Rb 85.47 1.53 Rubidium K α 13.396 L α 1.692	38 Sr 87.62 2.64 Strontium K α 14.165 L α 1.906	39 Y 88.91 4.47 Yttrium K α 14.958 L α 1.924	40 Zr 91.22 6.51 Zirconium K α 15.775 L α 2.044	41 Nb 92.91 8.57 Niobium K α 16.615 L α 2.169	42 Mo 95.94 10.22 Molybdenum K α 17.480 L α 2.292	43 Tc (98) 11.50 Technetium K α 18.367 L α 2.423	44 Ru 101.07 12.37 Ruthenium K α 19.279 L α 2.558	45 Rh 102.91 12.41 Rhodium K α 20.216 L α 2.697	46 Pd 106.42 12.02 Palladium K α 21.177 L α 2.838	47 Ag 107.87 10.50 Silver K α 22.163 L α 2.983	48 Cd 112.41 8.69 Cadmium K α 23.173 L α 3.133	49 In 114.82 7.31 Indium K α 24.210 L α 3.286	50 Sn 118.71 7.29 Tin K α 25.271 L α 3.444	51 Sb 121.76 6.69 Antimony K α 26.359 L α 3.604	52 Te 127.60 6.23 Tellurium K α 27.473 L α 3.769	53 I 126.90 4.93 Iodine K α 28.612 L α 3.938	54 Xe 131.29 0.006 Xenon K α 29.775 L α 4.110				
55 Cs 132.91 1.87 Cesium K α 30.973 L α 4.285	56 Ba 137.33 3.59 Barium K α 32.194 L α 4.466	57 La 138.91 6.15 Lanthanum K α 33.442 L α 4.647	58 Ce 140.12 6.77 Cerium K α 34.839 L α 4.839	59 Pr 140.91 6.77 Praseodymium K α 5.035 L α 0.927	60 Nd 144.24 7.01 Neodymium K α 5.228 L α 0.979	61 Pm (145) 7.26 Promethium K α 5.432 L α 1.023	62 Sm 150.36 7.52 Samarium K α 5.633 L α 1.078	63 Eu 151.96 5.24 Europium K α 5.849 L α 1.131	64 Gd 157.25 7.90 Gadolinium K α 6.053 L α 1.181	65 Tb 158.93 8.23 Terbium K α 6.273 L α 1.240	66 Dy 162.50 8.55 Dysprosium K α 6.498 L α 1.293	67 Ho 164.93 8.80 Holmium K α 6.720 L α 1.348	68 Er 167.26 9.07 Erbium K α 6.949 L α 1.404	69 Tm 168.93 9.32 Thulium K α 7.180 L α 1.462	70 Yb 173.04 6.97 Ytterbium K α 7.416 L α 1.526	71 Lu 174.47 9.84 Lutetium K α 7.655 L α 1.580					
87 Fr (223) 1.87 Francium K α 12.031 L α 2.732	88 Ra (226) 5.50 Radium K α 12.339 L α 2.806	89 Ac (227) 10.07 Actinium K α 12.652 L α 2.900	90 Th 232.04 11.72 Thorium K α 12.968 L α 2.996	91 Pa 231.04 15.37 Protactinium K α 13.291 L α 3.082	92 U 238.03 18.36 Uranium K α 13.614 L α 3.171	93 Np (237) 20.45 Neptunium K α 13.946 L α 3.250	94 Pu (244) 19.84 Plutonium K α 14.282 L α 3.339	95 Am (243) 13.69 Americium K α 14.620 L α 3.438	96 Cm (247) 13.51 Curium K α 15.113 L α 3.537	97 Bk (247) 14.79 Berkelium K α 15.613 L α 3.637	98 Cf (251) 15.1 Californium K α 16.113 L α 3.737	99 Es (252) 13.5 Einsteinium K α 16.613 L α 3.837	100 Fm (257) 15.1 Fermium K α 17.113 L α 3.937	101 Md (258) 15.1 Mendelevium K α 17.613 L α 4.037	102 No (259) 15.1 Nobelium K α 18.113 L α 4.137	103 Lr (262) 15.1 Lawrencium K α 18.613 L α 4.237					

Atomic number	Atomic weight
Density (g/cm ³)	Symbol
Element name	Energy (keV)
Spectral line	

Example: **Br**
35 79.90
3.12
Bromine
K α 11.924
L α 1.481

Handheld XRF

Innovation with Integrity

Appendix IV. Peak-Stripping Method of Background Estimation

- This method essentially compares the mean of the intensity counts between the neighboring channels, $y(x + w)$ and $y(x - w)$, and the current channel count $y(x)$.
- Here, w is the distance away from the current channel along the XRF spectrum energy axis.
- The general mathematical model for this method can be written as:

$$m(x) = [y(x - w) + y(x + w)]/2$$

- Let $m(x)$ be the mean value of channel x . If $m(x)$ is smaller than the actual count $y(x)$ of this channel, then the content of channel x is replaced by $m(x)$. This transformation is repeated until the background is reduced to an acceptable level.

Appendix VI. XRF Spectra Dataset (Peak intensities)

No	Lithology	S (Ka)	Mn (Ka)	Fe (Ka)	Co (Ka)	Ni (Ka)	Cu (Ka)	Zn (Ka)	As (Kb)	Ag (Ka)	Cd (Ka)	Pb (La)
1	Breccia	1.165	21	2312	12.63	12.6	22.7	29	7.7	12	14	8.5
2	Basic	1.182	27	1459	8.671	17.2	25	23	8.7	17	18	17
3	Basic	1.121	33	1990	13.84	21	21.4	45	13	16	17	32
4	Basic	1.277	163	9728	70.04	8.25	12.5	19	9.8	12	11	10
5	Basic	1.691	127	5047	41.6	13	12.9	24	11	12	11	15
6	Basic	1.359	17	1948	16.64	15	21.9	22	11	12	11	20
7	Basic	1.274	65	5666	42.66	21.6	20.4	26	12	11	12	12
8	Basic	1.661	55	5517	42.68	19.4	22	27	8.7	12	17	29
9	Basic	1.255	23	2906	23.63	22.1	22.5	21	9.4	14	15	14
10	Basic	1.975	61	6201	51.23	21.4	22.2	20	9.4	14	12	12
11	Basic	1.905	53	6348	49.77	25.5	19.6	26	12	12	12	14
12	Basic	2.014	56	6513	49.92	22.2	21.9	25	11	13	13	12
13	Basic	0.97	156	6284	47.34	16.4	14.7	27	8	12	12	13
14	Basic	0.954	22	5506	41.94	11.9	20.1	##	12	10	10	9.3
15	Basic	1.957	118	4814	37.9	20	13.8	24	9	10	13	11
16	Basic	1.048	38	4866	37.61	28.1	16.1	28	8.2	9.7	11	10
17	Basic	1.601	70	7235	53.88	23.5	23.8	23	9.5	10	12	12
18	Basic	1.214	56	6091	39.03	12.8	19.6	21	9.5	14	16	17
19	Basic	1.617	61	6054	45.65	28.1	19.9	26	16	12	14	41
20	Basic	1.962	85	7250	54.95	28.7	35.7	40	12	16	18	26
21	Basic	2.008	70	7253	62.07	28.9	27.6	41	16	13	13	39
22	Basic	1.682	74	6911	47.85	27	23	42	11	13	13	20
23	Basic	1.225	59	8798	68.95	14	16.9	31	13	13	12	31
24	Basic	1.096	37	6157	48.58	23.1	17.9	25	11	14	13	11
25	Basic	1.153	48	5656	40.07	14.5	14.9	15	7.9	12	12	9.7
26	Green Tuff	0.897	148	7005	50.56	24.4	22.3	29	8	11	12	9.9
27	Green Tuff	1.118	82	4777	33.61	14.2	20.9	31	11	14	14	13
28	Dacite	1.399	29	3420	26.52	18.2	23.4	43	11	15	16	21
29	Dacite	1.452	8.2	996.3	8.326	22.2	26.5	17	12	18	16	19
30	Dacite	1.349	16	2906	24.03	16.6	23.8	20	14	17	16	17
31	Dacite	1.518	17	3889	27.17	17.2	21.5	35	8.7	17	16	19
32	Dacite	1.411	21	2782	21.61	18.4	20.8	39	11	20	20	19
33	Dacite	1.562	20	2733	19.76	22	21.8	43	14	19	17	19
34	Dacite	1.747	12	2132	15.89	26	25.6	66	9.7	20	18	19
35	Dacite	1.304	5.4	1257	10.28	20.4	29.6	24	11	16	16	15
36	Dacite	1.618	36	2698	22.63	25.9	23.8	35	14	23	22	19
37	Dacite	0.967	14	2183	16.21	16.7	22	28	13	12	14	20
38	Dacite	1.032	44	3731	28.09	16.4	19.3	19	11	13	14	13
39	Dacite	1.343	29	2932	22.39	20.3	20.6	20	11	13	14	11
40	Dacite	1.12	19	4288	34.71	20.9	18.1	29	10	14	14	14
41	Dacite	1.315	14	2225	18.22	22	24.8	30	9	16	14	13
42	Dacite	1.983	19	2292	15.69	21.5	18.5	23	11	15	13	9.5

43	Dacite	1.88	14	4151	26.42	16.8	25.9	37	9.2	14	16	19
44	Red Lava	2.191	###	4396	19.24	11.4	11.4	21	140	12	12	43
45	Red Lava	2.176	423	6007	43.64	20.5	13.8	30	12	16	14	17
46	Red Lava	1.882	137	8232	58.34	15.3	15.7	26	9.2	12	15	10
47	Red Lava	1.071	79	6047	42.93	17.2	17	41	12	14	12	14
48	Red Lava	1.085	516	10363	72.84	17.9	16.4	37	10	10	11	13
49	B. Ryholite	1.314	51	857.5	9.906	16	18.7	15	11	16	18	17
50	B. Ryholite	1.122	19	1167	9.542	17	18.7	16	10	18	17	13
51	B. Ryholite	1.17	8.1	1226	8.74	21.1	21	15	14	16	13	16
52	B. Ryholite	1.153	11	1365	10.98	23	18.6	14	13	17	19	13
53	B. Ryholite	1.178	11	1373	10.71	20.2	17.6	16	13	19	17	14
54	B. Ryholite	1.208	30	1676	10.65	23.5	24.3	22	14	15	18	17
55	B. Ryholite	1.529	25	1308	10.78	20.3	21.7	19	12	15	13	17
56	B. Ryholite	1.067	33	2606	19.69	18.1	16.4	28	11	12	16	11
57	B. Ryholite	1.226	26	1700	13.67	23.5	17.5	27	11	15	17	16
58	B. Ryholite	1.109	11	920.2	5.796	19.6	13.3	24	9.9	13	16	9.5
59	B. Ryholite	0.975	12	1461	11.54	22	16.9	18	9.8	15	16	11
60	B. Ryholite	0.877	8.3	846.7	5.254	9.82	19.5	16	7.6	13	12	10
61	B. Ryholite	1.096	5.8	1322	8.764	15.4	24.4	14	10	16	15	13
62	Rhyodacite	1.158	9.3	835.9	2.466	17.8	21.7	28	13	12	15	33
63	Rhyodacite	1.197	62	963.9	6.509	15.7	24.1	37	12	13	14	50
64	Rhyodacite	1.205	17	859.3	2.313	15.6	24.7	44	19	16	17	76
65	Rhyodacite	1.228	15	1026	2.774	13.9	23.2	29	11	15	15	31
66	Rhyolite	1.451	12	1164	7.944	11.7	18	17	11	13	15	17
67	Rhyolite	1.284	15	851.3	5.128	18.2	22	27	13	17	16	24
68	Rhyolite	0.965	15	721.1	2.951	16.9	23.3	25	11	16	16	27
69	Rhyolite	1.113	15	969.2	6.41	12.6	21.1	25	11	15	18	23
70	Rhyolite	1.079	17	1618	7.878	16.6	27.2	31	11	16	15	21
71	Rhyolite	1.08	25	2511	10.33	13.5	25.8	27	8.5	14	15	15
72	Rhyolite	0.949	14	981.5	4.172	13.8	28.5	12	8.8	18	15	12
73	Rhyolite	1.294	21	1909	10.05	12.2	21.3	18	8.3	12	10	11
74	Rhyolite	0.916	17	1344	7.11	14.9	28.4	18	9.2	12	13	11
75	Rhyolite	0.992	6.1	1143	5.878	17.2	21.5	10	11	10	11	11
76	Rhyolite	0.805	17	1439	8.087	12.4	20	16	10	14	16	13
77	Rhyolite	1.336	19	1480	7.988	11.9	24.9	13	8.5	12	11	15
78	Rhyolite	1.05	22	2105	10.96	11.2	21.6	20	8.7	11	13	10
79	Rhyolite	0.95	5.4	1741	13.02	18.1	22.3	17	8.5	11	13	14
80	Rhyolite	0.841	25	1987	11.28	12.7	20.1	21	8.3	11	13	11
81	Rhyolite	1.186	9.6	2824	12.88	16.6	22.6	20	10	14	13	8.9
82	Rhyolite	0.995	12	1135	6.422	16.1	26.4	15	8.7	12	12	11
83	Rhyolite	0.942	20	1184	5.776	12.9	28.3	15	7.7	11	14	11
84	Rhyolite	1.131	10	928.3	3.927	12.2	24.8	16	8.3	15	15	14
85	Mas. sulfide	10.35	15	8279	51.6	9.17	2823	##	36	10	9.8	335
86	Mas. sulfide	11.83	14	9672	74.77	18.3	2653	##	20	9.7	9.7	403
87	Mas. sulfide	17.59	5	16321	110.2	4.48	1847	26	32	7.4	8.7	173
88	Mas. sulfide	12.68	63	13057	92	7.21	4673	56	41	9.5	10	210
89	Mas. sulfide	7.56	7.1	7605	57.71	6.98	155	19	9.8	11	10	30

90	Mas. sulfide	7.645	22	4207	41.12	37.3	84.7	##	23	6.6	6.8	529
91	Mas. sulfide	11.9	9.7	10611	80.42	27.1	3261	##	45	8.5	8.5	601
92	Mas. sulfide	18.36	3.1	16947	111.3	5.75	27.1	12	10	9.4	7.7	23
93	Mas. sulfide	4.342	3.9	3780	23.07	8.33	29.5	16	8.6	14	12	19
94	Mas. sulfide	3.382	2.4	2668	20.55	9.33	97.5	38	10	11	13	44
95	Mas. sulfide	6.941	2.2	6698	41.61	6.66	3103	44	15	9.9	10	69
96	Mas. sulfide	9.455	2.8	9177	69.73	7.5	2394	##	5.3	10	8.9	95
97	Mas. sulfide	10.02	28	6957	57.24	19	1494	##	28	11	13	556
98	Stockworks	3.861	5.1	2859	18.44	14.9	41.6	30	28	16	14	118
99	Stockworks	1.255	3.1	1450	8.998	11	25.9	17	5	11	9.4	13
100	Stockworks	2.383	3.2	1649	7.768	11.8	30	12	8.7	14	14	16
101	Stockworks	1.16	9	1257	6.763	14.9	30	##	7.4	14	13	116
102	Stockworks	1.087	9.1	3276	21.24	11.4	103	75	8.7	14	13	23
103	Stockworks	1.372	12	5271	29.26	10.8	30.5	##	6.9	15	14	13
104	Stockworks	1.806	3.4	954.8	6.396	12.4	24	8	10	15	14	15
105	Stockworks	2.118	3.1	1568	9.451	7.8	379	26	13	12	14	65
106	Stockworks	5.089	3.1	4728	33.37	7.92	560	18	6.6	11	11	27
107	Stockworks	5.217	4	3491	20.86	9.46	25.9	20	9	13	14	24
108	Stockworks	1.45	4.5	455.7	6.309	16.7	94.7	20	9.5	13	18	22
109	Stockworks	6.459	8.4	5802	41.23	5.46	17	18	6.2	9.4	7.5	19
110	Stockworks	1.786	9.2	2968	22.01	9.37	18.5	19	5.7	9.9	11	15
111	Stockworks	1.131	20	2382	16.25	6.79	13.5	22	4.6	8.2	9.7	11
112	Stockworks	1.131	57	3784	22.31	7.16	13.7	25	5.7	8.8	9.5	12
113	Stockworks	1.039	31	2056	15.13	4.63	14.1	29	4.7	8.3	9.2	9.5
114	Stockworks	2.794	111	6800	39.03	6.76	89.1	40	7.3	9.3	10	13
115	Stockworks	4.007	142	11500	79.66	9.05	14.2	30	4.5	9.2	9.3	13
116	Stockworks	3.004	36	4945	34.37	4.26	27.2	13	5.3	7.6	8.1	16
117	Shale	0.995	178	2524	13.41	14.9	22.8	18	7.9	12	13	19
118	Shale	1.455	55	1618	7.051	13.6	24.8	13	12	17	15	16
119	Shale	1.08	55	2154	8.518	10.3	15.1	18	9	11	13	13
120	Shale	1.456	66	4311	22.33	11.5	19.3	21	7.6	10	12	20
121	P. Shale	1.097	100	6131	36.24	20.7	21	29	9.5	15	14	16
122	P. Shale	0.896	278	4634	20.25	13.1	18.9	28	6	9.3	9.6	12
123	P. Shale	0.741	123	3382	18.48	13.1	16.1	23	6.5	10	9.8	12
124	P. Shale	1.255	536	4099	22.45	31.4	15.7	25	8.5	8.4	9.3	26
125	P. Shale	1.229	639	4183	22.73	42.4	17.7	28	23	11	11	93
126	P. Shale	0.93	141	5004	27.28	18.1	134	29	6.3	12	9.6	14
127	G. Tuff	1.004	109	2663	10.5	13	19.4	39	8.1	14	14	13
128	G. Tuff	0.962	242	3548	18.52	24.1	19.7	53	12	13	11	10
129	G. Tuff	1.119	144	2935	18.29	17.5	21.2	47	8	12	12	11
130	G. Tuff	1.259	195	2703	16.01	10.9	18.4	27	12	15	13	13
131	G. Tuff	0.96	270	2522	13.19	13.6	22.7	31	7.7	13	13	11
132	G. Tuff	1.256	54	1745	10.32	12.7	20.7	18	8.8	11	10	10
133	G. Tuff	1.311	43	1551	7.911	12.7	19.7	17	7.6	9.8	10	12
134	G. Tuff	1.348	29	1422	8.496	15.2	26	20	9.9	12	15	17
135	G. Tuff	1.215	233	2906	16.32	15.8	19.7	37	8.7	16	16	17
136	G. Tuff	1.248	292	4165	21.57	17.4	18	38	9.4	15	14	18

137	G. Tuff	1.091	33	2390	9.437	19.8	26	21	15	14	14	22
138	G. Tuff	1.559	29	2081	10.43	14.8	26.3	20	11	13	15	27
139	G. Tuff	1.147	38	4991	28.77	10.2	20.1	30	11	10	13	12
140	G. Tuff	0.801	697	3658	17.24	22.9	19.9	32	8.8	8.7	11	24
141	G. Tuff	1.027	599	4554	25.07	14.7	20.9	24	9.4	11	11	19
142	G. Tuff	1.016	61	2889	14.04	9.44	21.4	19	7.8	10	12	15
143	G. Tuff	0.938	96	2317	8.757	13.5	23	18	7.1	9.8	12	15
144	G. Tuff	1.336	22	2735	14.38	12.9	22	20	7.7	12	14	13
145	G. Tuff	0.993	84	3326	18.54	10	19.2	31	6.8	9.3	10	12
146	G. Tuff	1.024	117	2804	14.32	14.1	20.5	26	6.7	11	10	12
147	G. Tuff	0.748	225	3081	12.21	14.5	19.9	32	8	10	13	13
148	G. Tuff	0.989	268	5095	33.84	16	15.1	39	8.8	11	9.2	20
149	G. Tuff	1.113	22	2558	15.47	7.02	17.9	21	7.9	13	13	17
150	G. Tuff	2.44	42	2736	17.45	8	12.1	14	6.5	10	11	9.9
151	R. Tuff	0.92	27	1809	10.67	11.7	20.1	19	9.1	13	14	11
152	R. Tuff	1.087	23	1427	8.899	13.8	19.5	17	7.6	13	16	13
153	R. Tuff	1.042	19	1183	7.577	11.3	23.7	20	8.4	15	17	15
154	R. Tuff	1.112	12	2346	11.38	11.1	18.6	15	8.6	10	9.5	8.2
155	R. Tuff	1.318	10	746.9	4.074	9.51	21	17	8.8	13	13	15
156	R. Tuff	1.016	17	1226	6.572	11.5	23.9	17	8.9	14	14	14
157	R. Tuff	1.278	11	1867	12.64	15.7	24.5	21	8.4	14	14	16
158	R. Tuff	1.293	9.4	1823	10.33	10.9	26.2	39	9.9	16	13	14
159	R. Tuff	1.008	17	1778	11.83	10.9	19.2	13	7.5	12	10	12
160	R. Tuff	0.823	13	2873	16.98	11.6	21.7	18	7.1	11	11	8.9
161	R. Tuff	0.878	19	2277	13.73	11.7	24.8	28	8.6	11	12	14
162	R. Tuff	1.546	21	2201	11.81	17.6	25.3	47	10	14	15	35
163	R. Tuff	0.714	4.9	573.2	5.379	8.64	17.5	10	6.1	9.4	11	10
164	R. Tuff	0.932	11	710.2	5.433	11.6	17.6	12	6.4	12	9.4	9.3
165	R. Tuff	0.828	7.5	641.9	4.411	9.41	16	12	5.8	11	9.7	9.1
166	R. Tuff	0.795	11	1107	6.772	12.8	20	14	7.7	12	11	9
167	R. Tuff	1.115	4.4	851.6	4.281	17.8	22.8	31	9.8	15	15	26
168	R. Tuff	0.925	4.3	496.5	3.619	11.3	18.1	10	5.4	10	9.4	9.5
169	R. Tuff	0.857	4.4	732.2	6.317	7.94	16.7	9	7.5	10	11	11
170	R. Tuff	1.069	4.7	874.5	5.001	8.57	17.9	13	6.8	15	12	8.4
171	R. Tuff	0.93	21	1657	12.76	9.75	19.1	20	7.6	11	13	14
172	R. Tuff	1.195	5.5	396.9	5.177	6.99	14.3	10	5.9	8.6	8.3	10
173	R. Tuff	0.565	4.7	83.73	2.802	6.22	15.3	6	4.8	8.6	9.2	8.5
174	R. Tuff	1.278	16	1876	12.25	20.3	16.9	30	9.3	15	16	12
175	R. Tuff	1.18	41	2650	14.7	20.2	15.9	28	12	12	15	15
176	R. Tuff	1.213	43	4506	27.3	21.4	19.7	42	14	15	15	13
177	R. Tuff	1.027	14	1318	11.4	20.2	17.2	26	13	18	18	14
178	R. Tuff	1.336	30	3863	27.49	18.7	14.7	44	12	15	16	11

BIBLIOGRAPHY

- Almodóvar, G. R., Yesares, L., Sáez, R., Toscano, M., González, F., & Pons, J. M. (2019). Massive sulfide ores in the Iberian Pyrite Belt: Mineralogical and textural evolution. *Minerals*, 9(11), 653.
- A. Buhler and A. Seyfarth. X-ray fluorescence analysis for process control in the minerals and mining industries. *Bruker Report*, (145):20–22, 1998.
- Arias, M., Gumiel, P., Sanderson, D. J., & Martin-Izard, A. (2011). A multifractal simulation model for the distribution of VMS deposits in the Spanish segment of the Iberian Pyrite Belt. *Computers and Geosciences*, 37(12), 1917–1927. <https://doi.org/10.1016/j.cageo.2011.07.012>
- Beare, M. J., & Pittuck, M. F. (2006). *Aguas Teñidas Feasibility Study - Executive Summary*. Cardiff.
- Beckhoff, B., Kanngießer, B., Langhoff, N., Wedell, R., & Wolff, H. (Eds.). (2007). *Handbook of practical X-ray fluorescence analysis*. Springer Science & Business Media.
- Bergqvist, M., Landström, E., Landström, E., & Luth, S. (2019). Access to geological structures, density, minerals and textures through novel combination of 3D tomography, XRF and sample weight. *ASEG Extended Abstracts*, 2019(1), 1-3.
- Bruker, 2006, “Introduction to X-ray Fluorescence Analysis (XRF).”
- Corescan, Hyperspectral Core Scanning. Retrieved from <https://corescan.com.au/> on 07/06/2021
- DMT Group, Reliable results through high-resolution images: CoreScan3, 2021. Retrieved from <https://www.dmt-group.com/products/geo-measuring-systems/drill-core-scanner-dmt-corescan/dmt-corescan-3.html>
- Dalm, M., & Sandtkem, M. (2019). Geochemical mapping of drill core samples using a combined LIBS and XRF core scanning system. In *Real Time Mining-2nd International Raw Materials Extraction Innovation Conference in Freiberg, Germany*.
- De Vries, J.L., Vrebos, B.A.R., 2002. Quantification of infinitely thick specimens by XRF analysis,
- Van Grieken, R.E., Markovicz, A.A. (Eds.), *Handbook of X-Ray Spectrometry*, Second Edition. Marcel Dekker, New York, pp. 341–405.
- Dunlea, A. G., Murray, R. W., Tada, R., Alvarez-Zarikian, C. A., Anderson, C. H., Gilli, A., ... & Ziegler, M. (2020). Intercomparison of XRF core scanning results from seven labs and approaches to practical calibration. *Geochemistry, Geophysics, Geosystems*, 21(9), e2020GC009248.
- Erickson, A. J., & Padgett, J. T. (2005). Geological data collection. In *SME mining engineering handbook* (pp. 145–171).

- G. J. Weltje and R. Tjallingii. Calibration of XRF core scanners for quantitative geochemical logging of sediment cores: theory and application. *Earth and Planetary Science Letters*, 274(3):423–438, October 2008.
- Goff, K., Schaetzl, R. J., Chakraborty, S., Weindorf, D. C., Kasmerchak, C., & Bettis III, E. A. (2020). Impact of sample preparation methods for characterizing the geochemistry of soils and sediments by portable X-ray fluorescence. *Soil Science Society of America Journal*, 84(1), 131-143.
- Gullayanon, R. (2011). A calibration methodology for energy dispersive X-ray fluorescence measurements based upon synthetically generated reference spectra. Georgia Institute of Technology.
- Gumiel, P., Sanderson, D. J., Arias, M., Roberts, S., & Martín-Izard, A. (2010). Analysis of the fractal clustering of ore deposits in the Spanish Iberian Pyrite Belt. *Ore Geology Reviews*, 38(4), 307–318. <https://doi.org/10.1016/j.oregeorev.2010.08.001>
- Jackson, L. M. (2020). Mineralogical domaining of low grade and no grade zones using automated drill core logging (Doctoral dissertation, University of Tasmania).
- Jenkins, R., 1999. X-Ray Fluorescence Spectroscopy, Second Edition. Wiley & Sons, New York. 207 pp.
- Kruse, F. A. (1996). Identification and mapping of minerals in drill core using hyperspectral image analysis of infrared reflectance spectra. *International Journal of Remote Sensing*, 17(June 1996). <https://doi.org/10.1080/01431169608948728>
- Leistel, J. M., Marcoux, E., Thiéblemont, D., Quesada, C., Sánchez, A., Almodóvar, G. R. Sáez, R. (1997). The volcanic-hosted massive sulphide deposits of the Iberian pyrite belt review and preface to the thematic issue. *Mineralium Deposita*, 33(1–2), 2–30. <https://doi.org/https://doi.org/10.1007/s001260050130>
- Mahuteau, L. (2008). Study of algorithms for analysis of XRF spectra to automate inspection of carpets (Doctoral dissertation, Georgia Institute of Technology).
- Martin-Izard, A., Arias, D., Arias, M., Gumiel, P., Sanderson, D. J., Castañón, C Sanchez, J. (2015). A new 3D geological model and interpretation of structural evolution of the world-class Rio Tinto VMS deposit, Iberian Pyrite Belt (Spain). *Ore Geology Reviews*, 71, 457–476. <https://doi.org/10.1016/j.oregeorev.2015.06.006>
- Martin-Izard, A.; Arias, D.M.; Arias, M.; Gumiel, P.; Sanderson, D.J.; Castañón, C.; Sánchez, J. Ore deposit types and tectonic evolution of the Iberian Pyrite Belt: From transtensional basins and magmatism to transpression and inversion tectonics. *Ore Geol. Rev.* 2016, 79, 254–267.

Moreno, C.; Sierra, S.; Saéz, R. Evidence for catastrophism at the Famennian–Dinantian boundary in the Iberian Pyrite Belt. In *Recent Advances in Lower Carboniferous Geology*; Strogon, P., Sommerville, I.D., Jones, J.L., Eds.; The Geological Society: London, UK, 1996; pp. 153–162.

Niton, 2021, How xrf works. retrived from <http://www.niton.com>.

Orexplore, the GeoCore X10 is a very efficient assay lab-in-a-box,2021. Retrieved from <https://orexplore.com/what-we-do/geocore-x10/>

Quigley, M. A., & Yildirim, B. G. (2009). Mineral Identification and Domain Characterisation Using Two Automated Hyperspectral Core Logging Systems , Los Bronces Cu-Mo Porphyry Deposit , 1–4.

Reinhold Schlotz and Stefan Uhlig. *Introduction to X-ray Fluorescence (XRF)*. Bruker AXS Inc., Madison, Wisconsin, 2000.

Rene E. Van Grieken and Andrzej A. Markowicz. *Handbook of X-ray Spectrometry: Method and Techniques*. Marcel Dekker, Inc, New York, New York, 1992.

Rivard, B., Giles, D., & Tappert, R. (2011). Automated drill core logging using visible and near-infrared reflectance spectroscopy : A case study from the Olympic Dam Iocg deposit , South Australia. *Economic Geology*, 106(July 2015), 289–296.<https://doi.org/10.2113/econgeo.106.2.289>

R Jenkins, R W Gould, and D Gedeke. *Quantitative X-ray Spectrometry*. Marcel Dekker, New York, 1981.

R Jenkins. *X-Ray Fluorescence Spectrometry*. Wiley John and Sons Inc, second edition, May 1999.

R Scholtz and S Uhlig. *Introduction to x-ray fluorescence*. 2006.

SRK consulting. (2006). *Aguas Teñidas feasibility study*.

Sánchez-España, J., Velasco, F., & Yusta, I. (2000). Hydrothermal alteration of felsic volcanic rocks associated with massive sulphide deposition in the northern Iberian Pyrite Belt (SW Spain). *Applied Geochemistry*, 15(9), 1265–1290. [https://doi.org/10.1016/S0883-2927\(99\)00119-5](https://doi.org/10.1016/S0883-2927(99)00119-5)

S. D. Rasberry and K. F. J. Heinrich. Calibration for interelement effects in X-ray fluorescence analysis. *Analytical Chemistry*, 46(1):81–89, 1974.

Sjöqvist, A. S. L., Arthursson, M., Lundström, A., Calderón Estrada, E., Inerfeldt, A., & Lorenz, H. (2015). An innovative optical and chemical drill core scanner. *Scientific Drilling*, 19, 13-16.

Strauss, G. K., & Gray, K. G. (1986). Base metal deposits in the Iberian pyrite belt. In *Geology and Metallogeny of Copper Deposits* (pp. 304–324). Springer

Tornos, F. (2006). Environment of formation and styles of volcanogenic massive sulfides: The Iberian Pyrite Belt. *Ore Geology Reviews*, 28(3), 259–307. <https://doi.org/10.1016/j.oregeorev.2004.12.005>

Tornos, F., Lopez Pamo, E., & Sanchez España, J. (2008). The Iberian Pyrite Belt. Instituto Geológico Y Minero De España, (107), 1–31 pp.

Van Grieken, R., & Markowicz, A. (Eds.). (2001). Handbook of X-ray Spectrometry. CRC press.

Whateley, M. K. G., & Scott, B. C. (1996). Evaluation techniques. In Introduction to Mineral Exploration (2nd ed., p. 481). Blackwell publishing.

Yongdong Wang, Xinna Zhao, and Bruce R. Kowalski. X-ray fluorescence calibration with partial least-squares. Applied Spectroscopy, 44(6):998–1002, July 1990

Yousefi, B., Castanedo, C. I., Maldague, X. P., & Beaudoin, G. (2020). Assessing the reliability of an automated system for mineral identification using LWIR Hyperspectral Infrared imagery. Minerals Engineering, 155, 106409.